Theses and Dissertations | 1. Thesis and Dissertation Collection, all items

2015

Size-dependent mechanical properties and failure study of nickel nanoparticles

DelaFuente, Rene M.

Monterey, California: Naval Postgraduate School

http://hdl.handle.net/10945/49612

NAVAL POSTGRADUATE SCHOOL

MONTEREY, CALIFORNIA

THESIS

SIZE-DEPENDENT MECHANICAL PROPERTIES AND FAILURE STUDY OF NICKEL NANOPARTICLES

by

Rene M. delaFuente

March 2015

Thesis Advisor: Claudia C. Luhrs
Second Reader: Sarath K. Menon

Approved for public release; distribution is unlimited

THIS PAGE INTENTIONALLY LEFT BLANK

REPORT DOCUMENTATION PAGE	*Form Approved OMB No. 0704–0188*

Public reporting burden for this collection of information is estimated to average 1 hour per response, including the time for reviewing instruction, searching existing data sources, gathering and maintaining the data needed, and completing and reviewing the collection of information. Send comments regarding this burden estimate or any other aspect of this collection of information, including suggestions for reducing this burden, to Washington headquarters Services, Directorate for Information Operations and Reports, 1215 Jefferson Davis Highway, Suite 1204, Arlington, VA 22202–4302, and to the Office of Management and Budget, Paperwork Reduction Project (0704–0188) Washington DC 20503.

1. AGENCY USE ONLY *(Leave blank)*	**2. REPORT DATE** March 2015	**3. REPORT TYPE AND DATES COVERED** Master's Thesis	
4. TITLE AND SUBTITLE SIZE-DEPENDENT MECHANICAL PROPERTIES AND FAILURE STUDY OF NICKEL NANOPARTICLES		**5. FUNDING NUMBERS**	
6. AUTHOR(S) Rene M. delaFuente			
7. PERFORMING ORGANIZATION NAME(S) AND ADDRESS(ES) Naval Postgraduate School Monterey, CA 93943–5000		**8. PERFORMING ORGANIZATION REPORT NUMBER**	
9. SPONSORING /MONITORING AGENCY NAME(S) AND ADDRESS(ES) N/A		**10. SPONSORING/MONITORING** **AGENCY REPORT NUMBER**	

11. SUPPLEMENTARY NOTES The views expressed in this thesis are those of the author and do not reflect the official policy or position of the Department of Defense or the U.S. Government. IRB Protocol number ____N/A____.

12a. DISTRIBUTION / AVAILABILITY STATEMENT Approved for public release; distribution is unlimited	**12b. DISTRIBUTION CODE**

13. ABSTRACT (maximum 200 words)

The limited number of studies that focus on the size-dependent failure mechanisms of individual nanoparticles and their significance on epoxy composite material properties led to the twofold aim of this research: study the failure modes of nickel nanoparticles and determine the dependence of the mechanical properties of the Ni-epoxy composite on the size of the nickel particles used as reinforcement.

Samples of spherical nickel nanoparticles were separated by size based on their densities and the resulting sections used as reinforcement in epoxy composites. The microstructural characterization of the nickel samples were performed on a Scanning Electron Microscope and the mechanical properties of the different Ni-epoxy composite pucks investigated using a nanoindenter.

For the failure analysis investigation, an ultrasonic processor was used to induce damage to nickel nanoparticles of diverse sizes dispersed in a solvent. The corresponding effects of the treatment on the nanostructures were analyzed through X-ray diffraction techniques, to determine possible phase transformations, and Transmission Electron Microscopy, to analyze changes in the crystal lattice.

Findings indicate that the hardness and Young's Modulus values for the Ni-epoxy composites increase as filler particle size decreases and follows a normal Hall-Petch relation. The intense energy imparted by the ultrasonic process, along the particle-solvent interface, created a protective NiO coating in the Ni spherical nanoparticles. The latter seems to suppress the complete fracturing of the particle despite the creation of multiple lattice defects.

14. SUBJECT TERMS mechanical properties, nanomaterials, nanoparticles, nanotechnology, composite materials, failure mechanics, failure analysis, nickel nanopowder, lubricants, nanoindentation, hardness, Young's Modulus, epoxy, plasma synthesis	**15. NUMBER OF PAGES** 83
	16. PRICE CODE

17. SECURITY CLASSIFICATION OF REPORT Unclassified	**18. SECURITY CLASSIFICATION OF THIS PAGE** Unclassified	**19. SECURITY CLASSIFICATION OF ABSTRACT** Unclassified	**20. LIMITATION OF ABSTRACT** UU

i

THIS PAGE INTENTIONALLY LEFT BLANK

SIZE-DEPENDENT MECHANICAL PROPERTIES AND FAILURE STUDY OF NICKEL NANOPARTICLES

Rene M. delaFuente
Major, United States Army
B.A., St. Mary's University, 2003

Submitted in partial fulfillment of the
requirements for the degree of

**MASTER OF SCIENCE IN ENGINEERING SCIENCE
(MECHANICAL ENGINEERING)**

from the

**NAVAL POSTGRADUATE SCHOOL
March 2015**

Author: Rene M. delaFuente

Approved by: Claudia C. Luhrs
                   Thesis Advisor

                   Sarath K. Menon
                   Second Reader

                   Garth V. Hobson
                   Chair, Department of Mechanical and Aerospace Engineering

THIS PAGE INTENTIONALLY LEFT BLANK

ABSTRACT

The limited number of studies that focus on the size-dependent failure mechanisms of individual nanoparticles and their significance on epoxy composite material properties led to the twofold aim of this research: study the failure modes of nickel nanoparticles and determine the dependence of the mechanical properties of the Ni-epoxy composite on the size of the nickel particles used as reinforcement.

Samples of spherical nickel nanoparticles were separated by size based on their densities and the resulting sections used as reinforcement in epoxy composites. The microstructural characterization of the nickel samples were performed on a Scanning Electron Microscope and the mechanical properties of the different Ni-epoxy composite pucks investigated using a nanoindenter.

For the failure analysis investigation, an ultrasonic processor was used to induce damage to nickel nanoparticles of diverse sizes dispersed in a solvent. The corresponding effects of the treatment on the nanostructures were analyzed through X-ray diffraction techniques, to determine possible phase transformations, and Transmission Electron Microscopy, to analyze changes in the crystal lattice.

Findings indicate that the hardness and Young's Modulus values for the Ni-epoxy composites increase as filler particle size decreases and follows a normal Hall-Petch relation. The intense energy imparted by the ultrasonic process, along the particle-solvent interface, created a protective NiO coating in the Ni spherical nanoparticles. The latter seems to suppress the complete fracturing of the particle despite the creation of multiple lattice defects.

THIS PAGE INTENTIONALLY LEFT BLANK

TABLE OF CONTENTS

THIS PAGE INTENTIONALLY LEFT BLANK

LIST OF FIGURES

LIST OF TABLES

THIS PAGE INTENTIONALLY LEFT BLANK

LIST OF ACRONYMS AND ABBREVIATIONS

Å	Angstroms
A	contact area
a	Crystal Lattice Parameter
CdS	Cadmium Sulfide
CdSe	Cadmium Selenide
d	Crystal Lattice Spacing
E'	storage modulus
E''	loss modulus
E_c	complex modulus
E_i	Young's Modulus for the indenter tip
E_r	reduced Young's Modulus
GPa	Gigapascal
H	Hardness
h_c	contact depth
K	Thousand
keV	Kilo-electron Volts
kV	kilovolts
L	Liters
m	meters
mA	milliamps
mL	milliliter
mm	millimeter
N_2	Nitrogen
nm	nanometer
PDF	Powder Diffraction Files
P_{max}	maximum load
psi	Pounds per Square Inch
mm	Millimeter
nm	Nanometer
NNI	National Nanotechnology Initiative

PMC	Particle Matrix Composite
RPM	Revolutions per Minute
s	Seconds
SLPM	Standard Liters Per Minute
SEM	Scanning Electron Microscopy/Microscope
TEM	Transmission Electron Microscope
V	Volts
XRD	X-Ray Diffractometry/Diffractometer
μm	Micrometer

ACKNOWLEDGMENTS

This manuscript would not have been possible without the steadfast support, guidance, and encouragement of my instructor and thesis advisor, Professor Claudia Luhrs. Her infectious enthusiasm for Materials Science and Engineering inspires me to believe that even the smallest contribution to the Body of Knowledge is a contribution to shaping the future.

I would also like to thank Professors Sarath Menon and Chanman Park, without whose help, certain bodily and monetary injuries would have occurred.

Furthermore, I would like to thank my cohort group for their teamwork through the many late nights and long days. Special thanks to LTs Karima Greenaway and Jose Alberti.

Finally, thanks to my family and friends—all fortuitously in the local area and all with large donations in the love and support required through the trials of 21 months of higher education.

THIS PAGE INTENTIONALLY LEFT BLANK

I.   INTRODUCTION

A.   OVERVIEW

The history of nanotechnology began in the 1930s with the advent of the scanning electron microscope and its ability to magnify and resolve materials down to one billionth of a meter. These nanomaterials, as defined by the U.S. government's own National Nanotechnology Initiative (NNI), have morphological features smaller than 100 nanometers (nm) in at least one dimension. In the 1970s, Professor Norio Taniguchi coined the term nanotechnology during his research in ultra-precision machining; however, it was not until the invention of the Nobel Prize-winning Scanning Tunneling Microscope and the Atomic Force Microscope in the 1980s that the field of nanotechnology was able to develop as these machines gave the ability to see, manipulate, control, assemble, produce, and manufacture at the nanoscale [1].

The production of nanomaterials begins with either the reduction of bulk materials, called the top-down approach, or with growth from atoms and molecules, called the bottom-up approach. With manufacturing processes such as nanoimprint lithography, and chemical vapor deposition, to name a few, the unique, size-dependent properties of nanoparticles can be applied to metals, ceramics, polymers, and composites to suit any application. These size-dependent properties include thermal, optical, mechanical, magnetic, and electrical, and each property has direct multidisciplinary applications in chemistry, biology, physics, medicine, electrical, mechanical, computer, and materials engineering [2], [3].

The military benefits from advances in nanotechnology manufacturing. Whether it is lighter and more energy dense batteries and capacitors, lighter and stronger armor, or gold thin films on glass for reflecting heat and radar waves, military applications abound. As recently as 2013, the Special Operations Command was soliciting research into superhydrophobic coatings for electronics use underwater and dispensing with bulky containers and leaky seals [4]. Not only is nanotechnology in military and government use today; with the aim of remaining the world's leader in nanotechnology in the future,

the 2015 U.S. federal budget funded $1.5 Billion to the NNI to compete with the $1 Trillion global market in nano-related goods and services [5].

1. Size-Dependent Properties of Individual Nanoparticles

As mentioned previously, the thermal, optical, mechanical, magnetic, and electrical properties of nanomaterials are much different than their bulk counterparts. This is primarily due to the larger fraction of surface atoms [6] and surface area of the nanoparticles (Figure 1) [1], the high, unstable surface energy, and reduced imperfections. The high surface energy is attributed to fewer nearest neighboring atoms, dangling bonds exposed on the surface, and the resulting reduced bond distance between the surface and subsurface atoms. To reduce the increased surface energy, nanoparticles respond by shifting, restructuring, or adsorbing other atoms to the surface atoms.
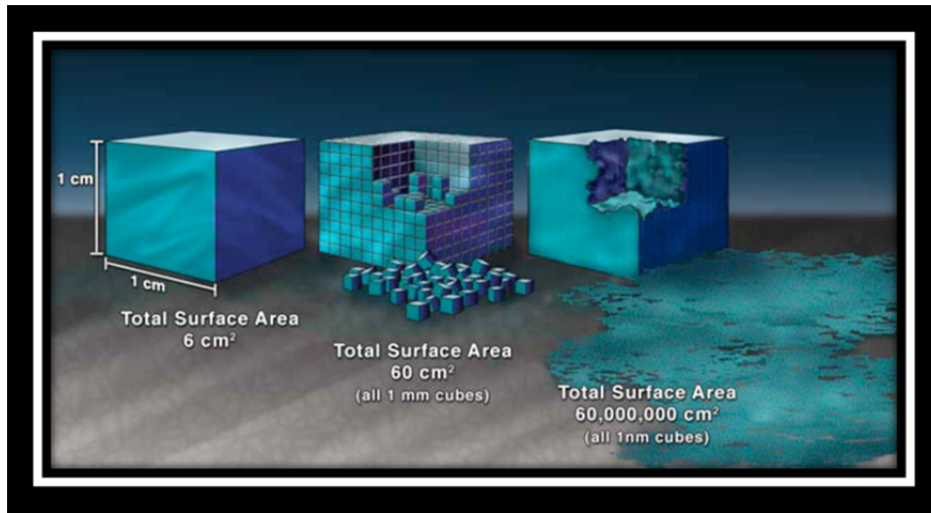
Figure 1.   Bulk vs. Nanoparticle Surface Area, from [1]

a. Thermal

The unique responses mentioned are what directly lead to lower melting temperatures. Melting point depression relates the decreasing size of a particle to its melting point (Figure 2) [7], and is a result of the larger surface-area-to-volume ratio. The larger surface area receives more of the energy while the lower volume can absorb less. This depression in the melting point of metal is more pronounced in nanoparticles less

2

than 100 nm and decreases rapidly below six nm, and can be expressed in the equation [7]:

$$T_m = T_{mB}(1 - 6\alpha \frac{r}{D}) \quad,$$

(1)

where T_m is the melting temperature of the nanoparticle, T_{mB} is the melting temperature of the bulk material, α is the shape factor, r is the radius of the atom, and D is the size of the crystal. Indeed, Kotrechko [8] reports that with increasing temperatures, an iron nanoparticle loses strength as a function of the square root of the temperature.
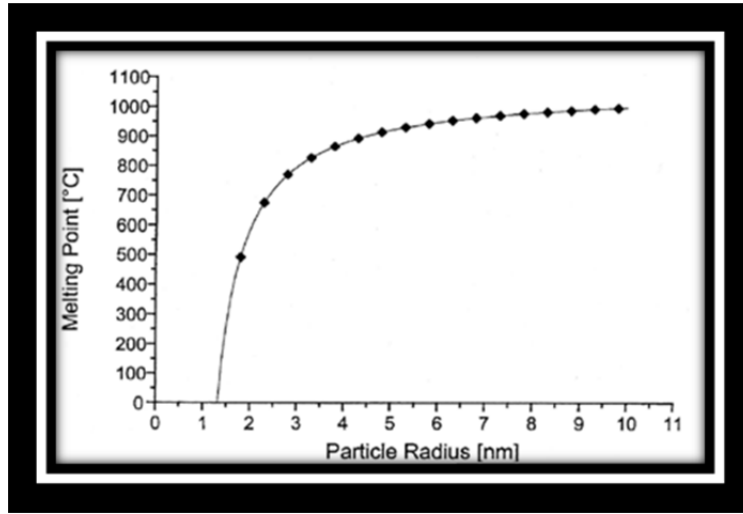
Figure 2.   Melting Point vs. Particle Radius for Metal Nanoparticles, from [7]

b.   *Optical*

Optical properties change with nanoparticles because of how their nanoscale size interacts with the larger wavelengths of visible light. These larger scale wavelengths are absorbed by the nanoscale particles, which then excite electrons across the varying band gaps of the varying molecules in the nanoparticle to the conduction band. The nanoparticles then emit energy as a function of their size and fluoresce a certain color according to the distance of that band gap as the electron returns to its original state in the valence band (Figure 3) [9]. Applications of this fluorescence are found in medicine and the electronics industry [9].

3
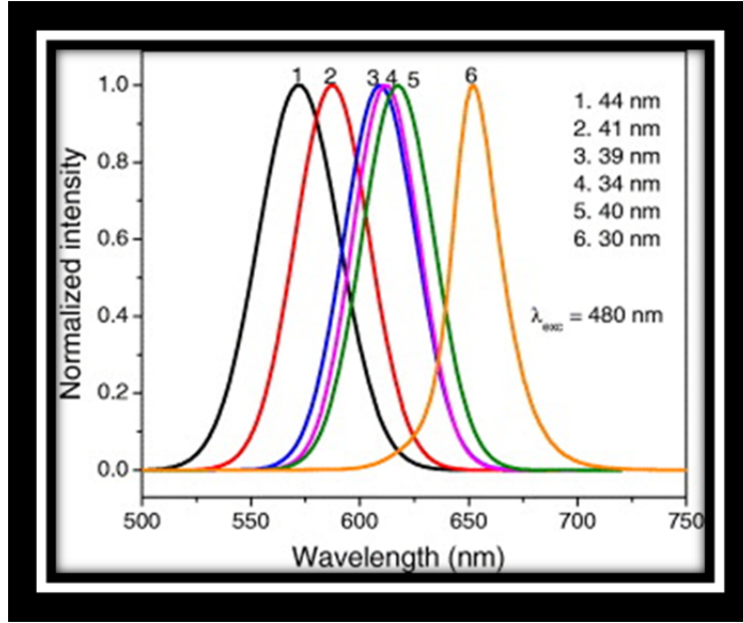
Figure 3.   Intensity/Wavelength Emission of CdSe/CdS Quantum Dots, from [9]

c.   *Magnetic*

Magnetic properties of nanoparticles have been studied since 1949 [10], however the superparamagnetic effect of magnetic nanoparticles is only relatively recent in its technological application. Part of this effect can be attributed to the large surface area inherent in nanoparticles. For example, particles with diameters of 10 nm can have large magnetic moments (over 10,000 Bohr magnetons greater than bulk materials), at lower temperatures [11]. The benefits of this effect can be seen with higher and higher magnetic data storage densities for the electronics arena and sensors for medical imaging and military sensors.

d.   *Electric*

The electric properties of nanomaterials have impressed scholars and technologists for years. With high rates of conductivity due to tunneling currents overcoming any resistivity between contacts, nanomaterials such as graphene or its counterpart, the carbon nanotube, have been increasingly studied for use in capacitors and circuitry. Meanwhile quantum dots of Gallium Arsenide are used for the most complex semiconductors and the naturally occurring silica is used in insulators. Interestingly, there

4

is such a thing as too small. It has been found that below a certain size for metallic nanoparticles, the dielectric constant begins to drop off with a corresponding drop in conductivity [12].

e.   Mechanical

While the mechanical properties of composites containing nanofillers are abundant, there is a limited amount of research and data on the mechanical properties and deformation mechanisms [13] of individual nanocrystalline metals and other nanoparticles. Results have relied on computer modeling [14] since deformation experimentation of nanoscale particles has proven difficult due to the lack of established techniques, equipment, and the difficulty in manipulation. While deformation mechanisms in bulk, and even in micron-scale materials are well studied, there is an anomalous relationship to the nanoscale [15].

For the bulk materials, the Hall-Petch relationship mathematically details yield strength to grain size, and in general, the smaller the grain size, the higher the yield stress and fracture resistance. Under 20 nm, however, there is an almost inverse relationship where strength actually decreases—called the inverse Hall-Petch (Figure 4) [16]. Plastic deformation in nanoparticles can be attributed to sliding or migration of the grain boundaries from diffusion or atom shuffling. In bulk materials these grain boundaries remain static and are a barrier to movement of dislocations [17]. This thesis attempts to add to the body of knowledge in this area.
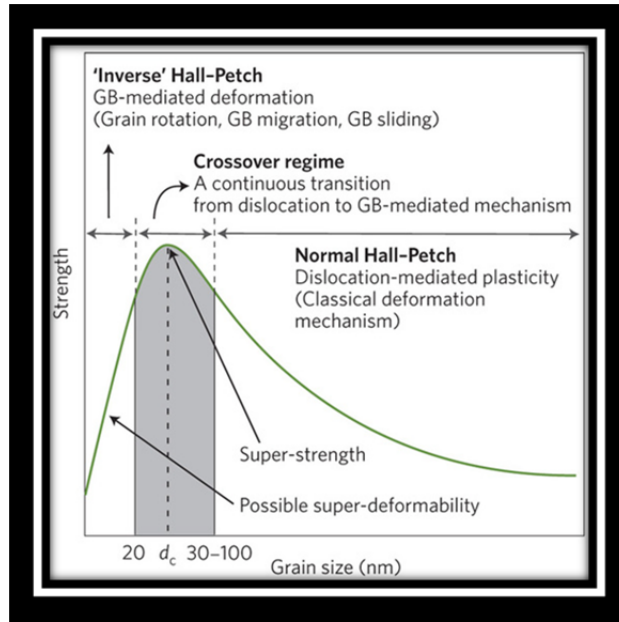
Figure 4.   Hall-Petch Relationship in Bulk and Nanomaterials, from [16]

2.   Mechanical Properties of Composites

Compared to metallic and ceramic matrices, polymeric matrices have a more complex chemical structure and relationship to their reinforcement. Composed of long chains of covalently bonded molecules, polymers are poor conductors of electricity and are not as strong, rigid, or tough. They are however, cheaper and easier to work with. Indeed, polymers can have elastic constants much lower than metals or ceramics; yet their elasticity is dependent on temperature and time. According to the Struers Speci-Fix product description, the epoxy used in this thesis, consists of a Bisphenol-A resin and a Benzyl alcohol-based curing agent, forms the stronger, more rigid, cross-linked polymer.

Composite types can be described by the matrix or the type of reinforcement. Matrices can be many types of materials such as metals, alloys, glasses, ceramics, or polymers, while reinforcement types can be either particle, short fiber, continuous fiber, or laminate. The polymer matrix composite (PMC) created in this study uses nickel nano- and micron-sized particles as its reinforcement to strengthen, harden, toughen, elasticize, and increase the heat capacity of the composite without an appreciable gain of mass [18].

Indeed, the addition of any reinforcement changes the characteristics of the matrix while the reinforcement itself only changes in rare circumstances. The reinforcement mechanism can be likened to concrete where granules are introduced into cement to stop crack propagation. To further explain this reinforcement mechanism of nanoparticles on toughness, Rajagopalan [18] discusses the fact that the nanoparticles induce a change from an intergranular crack mode to a transgranular mode.

Kutvonen et al. [19], model the effect of size, loading, and shape on polymer nanocomposites and relates three types of interactions in a PMC to mechanical properties. The weakest is the nanoparticle to nanoparticle interaction followed by the polymer to polymer interaction. The strongest interaction belongs to the polymer to nanocomposite interaction. The results of this modeling show that the smallest particles have more pronounced effects over particle shape, while over-loading leads to a weak and defective composite.

The creation of defects would occur primarily during synthesis, and are of particular importance in this study due to the processing required during experimentation. The three main defects to mitigate in the composite portion of this study are: voids caused by trapped gasses; inadequate dispersion of the reinforcing nanoparticles; and microcracks forming from excess moisture in the system. Meticulous quality control should mitigate these concerns.

As mentioned previously, diverse material properties suffer dramatic changes when materials reach the nanometric size. Given the limited number of references encountered when searching for individual particulate failure modes and the critical sizes at which macroscopic materials deviate from their expected behavior, this work aims to study the most significant changes suffered by nickel nanoparticles when subjected to ultrasonic horn treatments and their size dependence. We also study the changes in the nickel-epoxy composite mechanical properties when diverse sizes of reinforcement are employed.

7

3.   Thesis Goals and Objectives

With the changes in properties of nanoparticles and their composites noted above, several questions arise. We have divided those into two categories, the first one related to explore the properties of spherical nanoparticles in the absence of a matrix, and the second one regards the influence of the spherical particles size on the properties of their epoxy composites. From these questions we expect to learn what strategies could be followed to improve the mechanical properties of individual particulates.

Category I:

- Is there a satisfactory way to manipulate, test, and characterize the damage induced on the individual nanoparticles?
- Are testing and the testing parameters adequate to cause particle damage that can be identified with the tools available?
- If the nanoparticles do not fail or present more resistance to damage, is it possible to identify the mechanism of their resistance?
- Is there a process to synthesize nanoparticles with potential to produce structures that can withstand the damage?

Category II:

- How do we test the performance of the composite?
- Will there be an appreciable difference between the reinforcing properties of different sizes of particles in an Epoxy Polymer Matrix Composite?

The data presented in the next chapters will provide the answers to questions in category I, which, along with previous research, confirm that there are some strategies to manipulate, test, and characterize the failure modes in nanostructures. These strategies are not based on direct measurements but in the study of the causes and effects of using treatments meant to incur damage on the samples and the observations of these effects on the microstructure and phases present in the postmortem specimens. It has been identified that, in the proper conditions, the use of an ultrasonic horn could provide sufficient energy to induce damage. Microwave plasma methods carried out in atmospheric conditions seem to be an effective way to generate spherical particulates of diverse sizes.

Modeling studies of the influence of size, loading, and shape on the mechanical properties of composites by Kutvonen et al. [19] give some direction to answering the questions posed in category II. While not following the testing methods modeled in that

study, this thesis will experimentally attempt to determine any differences between sizes of reinforcement and mechanical properties of PMC. It is hoped to correlate the experimental results using available equipment to those results acquired through computer modeling.

The goals of this thesis are then twofold: the first is to study the failure mechanisms at the individual nanoparticle level, while the second is to study the relationship between the mechanical properties of the polymer matrix composite and its dependence on the size of the nickel nano- and micron-sized particles used as reinforcement. The path that led to these goals is shown in Figure 5.
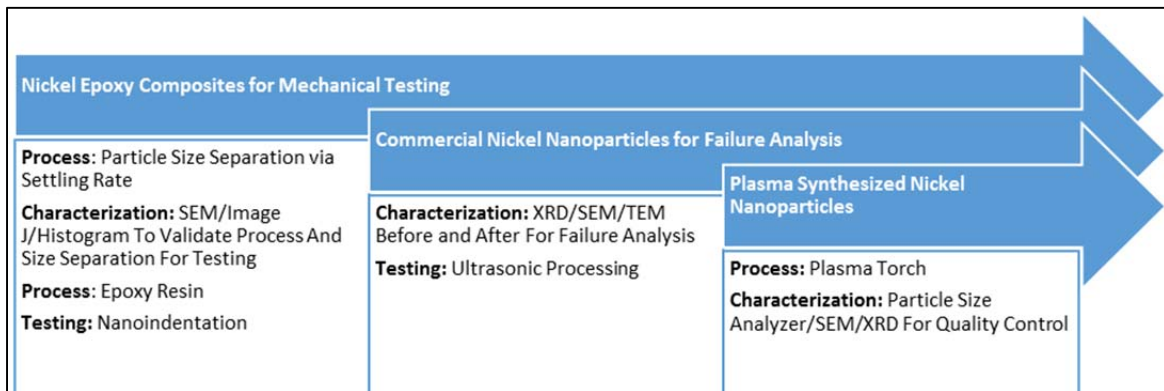

Figure 5.   Thesis Flow and Way Forward

THIS PAGE INTENTIONALLY LEFT BLANK

II.   EXPERIMENTAL PROCEDURE

To achieve the goals stated in the previous chapter, this study begins with the manipulation and processing of commercial nickel nanoparticles to achieve size distribution separation through differences in settling rate. Characterization follows to assess the size distributions of the different samples produced before mixing them with the epoxy polymer precursors. Introduction of the nanoparticles in the polymeric matrix is then followed by the determination of the mechanical testing of the composite.

Failure induction is then attempted at the individual nanoparticle level by testing the commercial nickel nanoparticle with an ultrasonic liquid processor. This is followed by further characterization of the nanoparticles using two electron microscopy techniques and x-ray diffractometry. Finally, the synthesis of highly spherical, defect-free particles, are conducted using a microwave plasma system. The following paragraphs provide more detail on how these operations were conducted.

A.   SAMPLE PREPARATION

Sample preparation was an obvious and necessarily meticulous beginning to experimentation. As the foundation to the experimentation and characterization that followed, much trial, error, and refinement were required prior to processing the tested samples. In this study, size separation of the commercially available nickel nanopowder was required prior to loading into the epoxy matrix.

1.   Particle Size Separation in an Ethanol Medium

Aldrich 577995 Nickel nanopowder is a dark gray powder with a density of 8.9 grams per milliliter (g/mL) and manufactured with an average size distribution of 100 nanometers or less. Bulk nickel, with an atomic number of 28, is a silvery, malleable, ferromagnetic metal which forms face centered cubic (fcc) crystals at temperatures below 1700K at sea level pressure (Figure 6) [20]. Settling rate was the method used to separate the particles, with a goal to separate into three separate size distributions in the range of

less than 100 nanometers. In this method, it is assumed that each nickel nanoparticle has the same density; hence their masses will be proportional to their sizes.
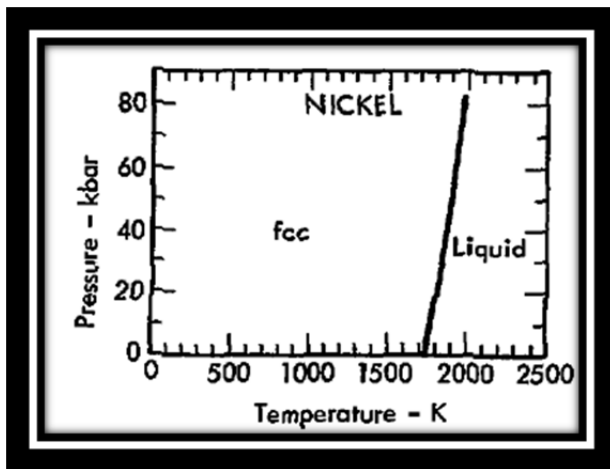

Figure 6.   Phase Diagram of Nickel, from [20]

We use this proportionality to relate the settling rate with size, as the larger and heavier particles will settle faster than the smaller and lighter ones. It is important to note that the differences between the frictional forces of different diameters were deemed negligible due to the nanoscale differences between particles in an ethanol medium. Compared to deionized water, which has a density of one gram per milliliter and a molecule size of 0.28 nanometers, ethanol is less dense at 0.789 g/mL and a molecule size of 0.44 nanometers [21], making it a more suitable media to disperse nanoparticles.

To determine the proper timing and size distribution for this method, the first effort used 25 milliliters of ethanol poured into a graduated cylinder and 199 milligrams of the nickel nanopowder. The graduated cylinder was then placed in a Bransonic 2510R Ultrasonic Cleaner (Figure 7) for two minutes to ensure complete dispersion of the particles and allowed to settle for 15 minutes. In three milliliter increments, the mixture was pipetted into five separate vials and placed into the ventilation hood to settle further overnight. All of the particles settled to the bottom and most of the remaining ethanol was pipetted away leaving nickel sediment of varying opacity in the bottom of the vial. The sediment was then dried and prepared for scanning electron microscope observation.

Figure 7.   Graduated Cylinder in Ultrasonic Cleaner

From this first run, techniques were refined in the following two runs to consume less ethanol, achieve larger yields for the smaller particles, and accelerate drying time. To recover more ethanol and increase the yield, the final run used three grams of nickel filtered through a 63 micron sieve (Figure 8) to isolate the largest aberrant particles. Four samples were then drawn from a separatory funnel (Figure 9) for the final settling run: the first sample, consisting of the largest particles, was drawn at three minutes elapsed time; the second at five minutes elapsed time; the third sample, consisting of the smallest particles, were drawn at eight minutes elapsed time; and after rinsing the glassware, the collected residue was collected as the fourth sample.
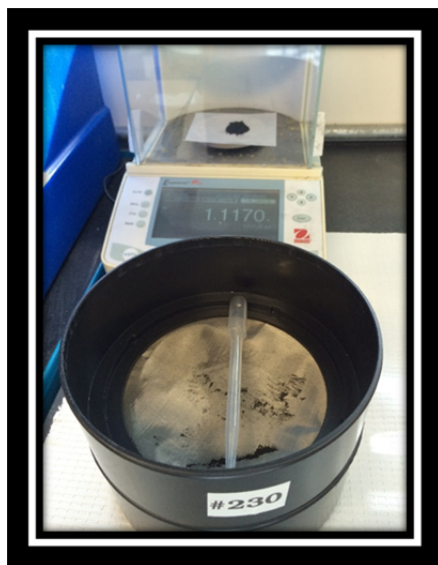
Figure 8.   #230 Sieve (63 micron)
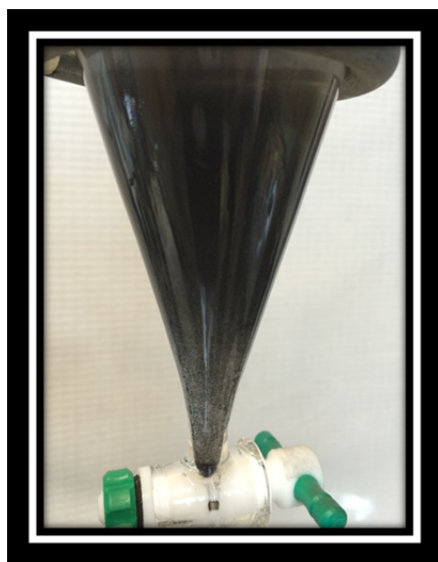
Figure 9.   Separatory Funnel Used for Nanoparticle Separation by Settling Rates

The four samples were then placed into a Hermle Labnet Z206A Centrifuge (Figure 10) and set to 2000 rpm for five minutes to separate the solid from the liquid. The majority of the ethanol was then pipetted away and the remaining slurry was poured into evaporating dishes then placed into the drying oven at 70°C to accelerate evaporation times. The nickel residue was dried, and then weighed, to measure yields and compute the amount of epoxy required.

Figure 10.   Hermle Labnet Z206A Centrifuge

2.   Composite Production

Struers Speci-Fix 20 epoxy mix Kit (Figure 11) was used as the matrix for the hardness and Young's Modulus evaluation by forming composite pucks with 1% of the nickel powder by weight. Six of these epoxy matrix pucks were tested: one puck acted as the control with no added powder; the second puck consisted of the particles less than 50 nanometers; the third had approximately 50 nanometer sized particles; the fourth had the approximately 100 nanometer particles, the fifth one using the unfiltered mix of commercial nanopowder; and the final one used micron sized Aldrich nickel powder.
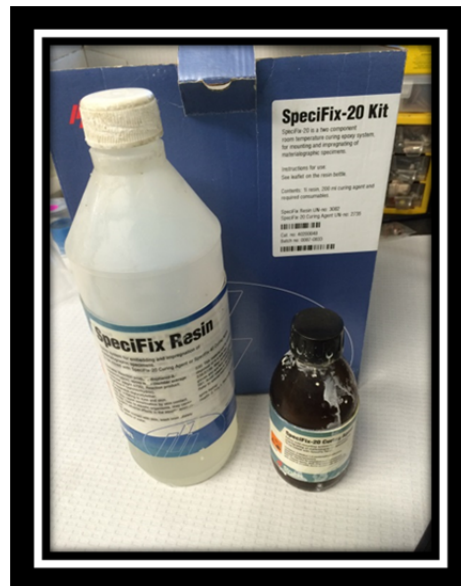

Figure 11.   Struers Speci-Fix 20 Epoxy Mix

Preparation of each composite puck required meticulous care at each step due to the limited amounts of filler sample and the adhesive properties of the epoxy matrix. A seven to one ratio by weight of resin to curing agent was required for the control sample containing no filler. For the epoxy samples loaded with nanoparticles, and as a technique to mitigate bubble formation in the resin and fully disperse the reinforcing particles, the resin was poured into a plastic mixing cup or evaporation dish containing the nickel powder, then placed in the ultrasonic cleaner and mixed with a stirring stick for five minutes. The container, resin, and nickel were then placed into the scale and the curing agent added in the proper ratio. The entire mixture was then placed back into the ultrasonic cleaner and mixed for another 5 minutes then poured into a lightly lubricated 1.25-inch reusable two-piece plastic mold.

The composite puck with commercial mix consisted of 80 milligrams of the unfiltered commercial sample mixed with seven grams of resin and one gram of curing agent. The heavier 100+ nanometer particles collected in the first sample also gave the largest yield, and 80 milligrams of this was collected from the evaporating dish into a plastic mixing cup, and eight grams of the resin and curing agent were added in the process mentioned previously. The yields of the second, third, and rinse samples were 65, 17, and 15 milligrams, respectively. Due to the low yields and identical size distributions, Sample 3 and the rinse product were mixed together. A one weight-percent ratio of nickel yield to epoxy was then mixed, as shown in Table 1.

Table 1.   Epoxy Puck Compositions

Sample	Nickel Particle Size (nm)	Nickel Yield (mg)	Resin Added (mg)	Curing Agent Added (mg)
Control	n/a	0	49000	7000
Micron	≤ 5000	560	49000	7000
Mix	≤ 100+	80	7000	1000
1	99	80	7000	1000
2	37	65	5687.5	812.5
3	47	17	1487.5	212.5
Rinse	51	15	1312.5	187.5

As each of the epoxy composites only partially fill the 1.25 inch, 27 mL plastic mold, this first layer was allowed to dry for 24 hours and then a 7:1 epoxy only solution was added to this hardened layer in the mold. The epoxy composites were then allowed to cure for a further 96 hours. The completed pucks were then hand ground and polished using 240-, 320-, 400-, and 600-grit sand paper, then polished using a polishing wheel and 0.05 µm alumina solution (Figure 12).
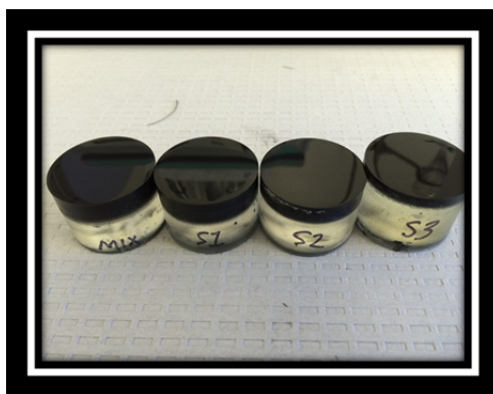

Figure 12.   Polished Epoxy Composites

3.   Aerosol-Through-Plasma Microwave Torch

As an alternative to off the shelf nanoparticles, solid spherical nanoparticles of nickel were prepared using aerosolized Aldrich 266981 5µm Nickel powder with argon gas in a microwave plasma torch. This aerosol-through-plasma (A-T-P) technique [22],[23] occurs in near atmospheric pressure and directly results in the transformation of the precursors to solid spherical particles due to the +3500°C temperatures that rapidly melt the particles and to the fast convective cooling (Figure 13). Phillips et al. [22], report that the high temperatures during processing are beneficial in aiding the temperature stability of the spherical nanoparticles produced which, in turn, aids in increasing the temperature at which these particles sinter and agglomerate.

Figure 13.   Atmospheric Microwave Plasma Torch System

Microwaves were generated using 901 watts from an 1100 watt Astex magnetron (Figure 14a) [23]. Simultaneously, 5.17 Standard Liters Per Minute (SLPM) of argon gas from the plasma gas inlet was inducted into the lower portion of the quartz chimney and ionized as it crosses the microwave waveguide (Figure 14b) [23]. Concurrently, 1.615 SLPM of argon gas from the aerosol inlet was inducted into a 5mL beaker containing 15.527g of the nickel powder. To promote even dispersion, this nickel containing beaker is immersed in the Ultrasonic Cleaner during the entire process. The aerosolized mixture from this beaker is then forced upward (Figure 14c) [23] through the central alumina tube and into the ionized plasma zone within the quartz torch creating a green-tinted glow. The aerosolized spherical nanoparticles then convectively cools and is pulled through a slightly negative pressure area (10 torr below atmospheric pressure) and collected on filter paper, yielding 0.17g.of fine black powder (Figure 15).
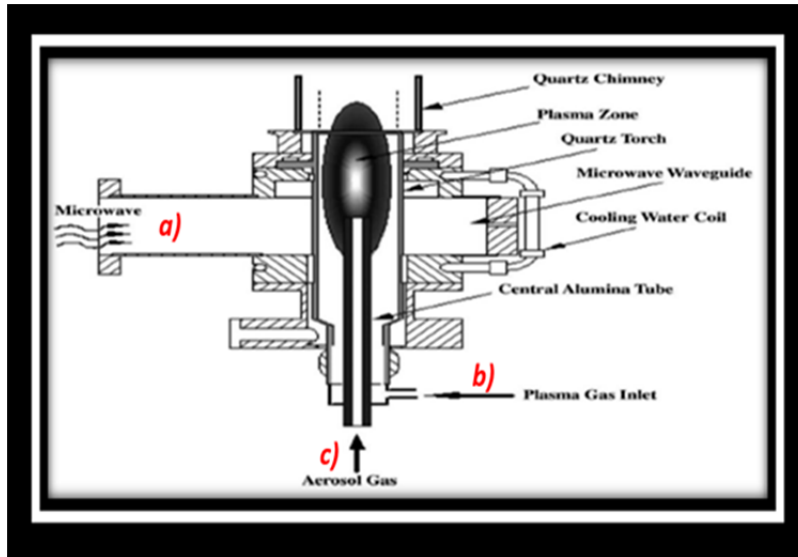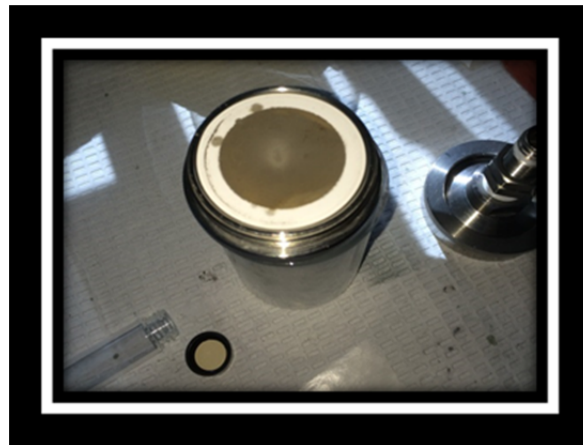
Figure 14.   Microwave Torch, from [23]

Figure 15.   Microwave Plasma Filter Product

B.   CHARACTERIZATION

As mentioned in the Introduction, characterization at the nanoscale can be difficult, however with practice on the appropriate equipment, entirely possible. Various advanced techniques of microstructural characterization were employed in this thesis during sample preparation, prior to composite synthesis, and after failure induction. The techniques employed included SEM, STEM, TEM, XRD, and PSA, and characterization at these points validated methods used to prepare the samples, verify purity of the

commercial control, and assess failure and correlate failure modes after Ultrasonic Testing.

1. Particle Size Analyzer

A Horiba Partica LA-960 Laser Diffraction Particle Size Analyzer was used as an attempt to measure the mean average particle size in the samples as well as the size distribution (Figure 16). In theory, as a particle of a certain diameter is struck, light is diffracted, and the intensity of the diffracted light is measured considering the particle's diameter, circumference length, and diffractive index, as well as the wavelength of the incident light. Angles of diffraction are also important considering that smaller particles have larger scattering angles and vice versa. Particle size distributions are calculated based on these collected angles and the diffracted light intensity, which is inversely related to the particle size. As a technique for laser diffraction, this instrument uses a red laser and blue LED light source, a fraction cell consisting of the sample and dispersant, a photodiode array to detect the diffracted light, and the software to calculate the particle size and distribution from the effects of the diffracted light (Figures 17and18) [24].

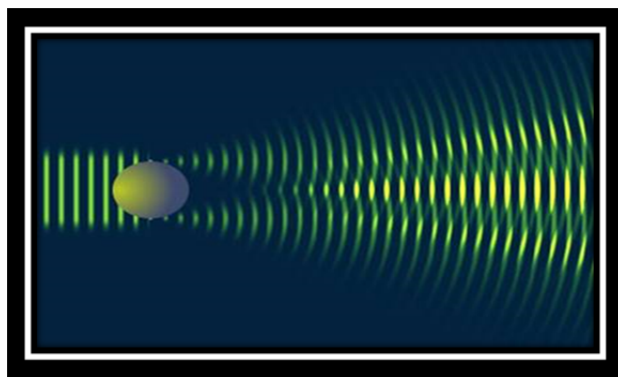

Figure 16.   Horiba Partica LA-960

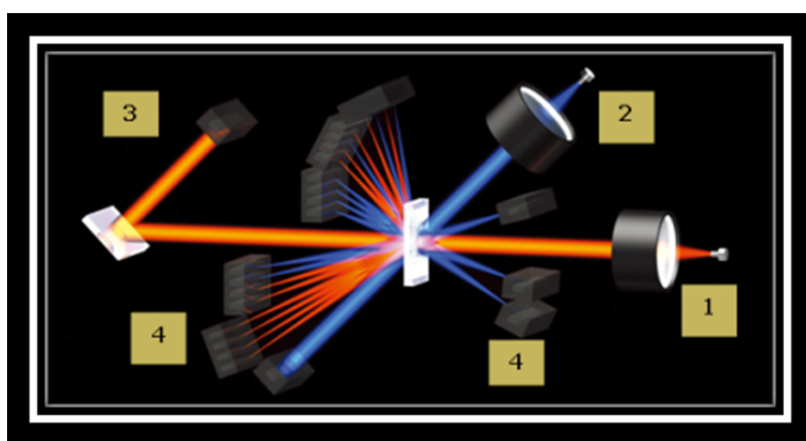Figure 17.   Light Diffraction around a Particle, from [24]

Figure 18. Particle Size Analyzer Light Diffraction and Collection Array, from [24]

Our sample was dispersed in a sonic bath for 30 minutes prior to analysis to separate any agglomerations, then five milligrams of the nickel sample were added to a 10 mL vial and filled with deionized water for the first run and isopropanol for the second run. Deionized water or isopropanol were then used to fill the fraction cell. The conditions required setting the sample refractive index of nickel to 1.9 and sample imaginaly index to 3.7. Deionized water had a dispersant refractive index of 1.333 while isopropanol had a dispersant refractive index of 1.378. A distribution of numbers-based statistical modeling was programmed, and then the sample solution was pipetted into the fraction cell until the instrument showed that transmittance was within range of detection and five measurements were taken (Figure 19).

Figure 19.   Nickel Solution in Fraction Cell

2.   Scanning Electron Microscope

A Zeiss Neon 40 scanning electron microscope was used to determine the nickel nanoparticle topography, morphology, and size distribution. Due to the sensitive nature of the field emission electron gun, electromagnetic lenses and coils, sample preparation focused on ensuring dryness after the exposure from the wet mediums and with ensuring an even layer of sample covered the carbon tape to reduce the effects of charge-built up. Desiccation of the sample was facilitated using the drying oven at 40°C prior to placement in a vacuum desiccator for 24 hours prior to the SEM examination.

The 30 μm aperture was used with a working distance of five mm. Electron beam currents ranged from 2–20 kV. Quantitative stereological analyses of the SEM images were performed to determine sample size distribution. Evaluation of these images required the use of commercial ImageJ and SAS Institute's JMP statistical software.

3.   X-Ray Diffraction

X-ray diffraction (XRD) was conducted using a Rigaku MiniFlex 600 diffractometer using a copper anode (Figure 20). Used in part to determine crystal structures of many crystalline samples, observed diffraction patterns are compared to

those of previously compiled powder diffraction files (PDF) by the International Centre for Diffraction Data (ICDD). XRD was used in this study to identify the phases in each sample, detect oxidation, and verify quality control during the microwave plasma synthesis.

Figure 20.   Rigaku MiniFlex

XRD begins when an electrical current is applied to an x-ray vacuum tube containing, in this case, a tungsten cathode filament and copper anode. The deceleration of the electrons from the cathode by the Cu target (anode) produces x-rays which are released through beryllium windows in the x-ray vacuum tube. These x-rays are then aimed at the now irradiated sample. The geometric Bragg-Brentano $\theta/2\theta$ arrangement used here together with the 1D detector generates a high quality diffraction pattern in a few minutes of acquisition time. Once measured these patterns are compared to those of the ICDD compiled standards and the Rigaku PDXL software is used to analyze the experimentally determined X-ray diffraction pattern.

Differentiation between Nickel (Ni), Nickel Oxide (NiO), and Nickel (III) Oxide (Ni_2O_3) species in our samples was a specific concern. Each sample was poured into the zero background silicon stage and packed evenly into the small cavity and ensuring a flat sample surface using a glass plate. Start and end 2θ positions of 20–90, a step width of 0.02 degrees, a scan speed of 10°/min, a current of 15 mA, and voltage of 40kV, were the

parameters programmed before each sample was tested. The Rigaku Software then measured the geometry of the diffracted x-rays and compared these results to the standard PDF cards on file.

4. Transmission Electron Microscope

To determine the effects of the ultrasonic tester and determine changes to the crystal lattice, composition and particulate morphology, a transmission electron microscope (TEM), 200 kV FEI Osiris was used. Each sample was dispersed in ethanol and a drop of each was allowed to dry on a lacey carbon-copper 200-mesh grid (Figure 21). Each carbon-copper grid were then placed into the TEM and examined at 200KV using bright field images and high resolution imaging techniques.

Figure 21.   Air-Drying Copper Grid (Held by Tweezers) and Sample Vial

C.   MATERIAL PROPERTIES TESTING - NANOINDENTATION

The Agilent Nanoindenter G200 was used to measure the hardness and Young's Modulus of the control epoxy puck and the small-, medium-, and mixed-sized nanoparticle epoxy composite pucks. Using an electromagnetic assembly to actuate an indenter tip (Figure 22) [25], the nanoindenter can resolve displacements of less than 0.01 nm and is capable of loads of up to ten Newtons [25]. The sensitivity of the assembly also detects the elastic and inelastic properties of the material as the indenter is pushed into, and subsequently pulled out of, the surface. The precise nature of the

nanoindenter allows for the minimal use of material and allows for either multiple tests or a small amount of material used. In this test, the large surface area of the epoxy pucks, as compared to the nanoindenter tip gave the ability to select a 20-point array for a better sample size and still have room for follow on tests.
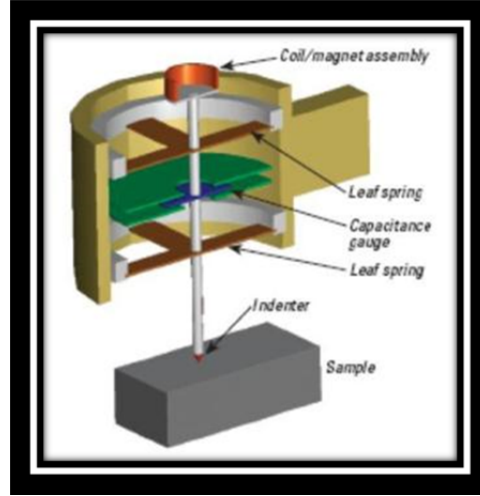

Figure 22.   Nanoindenter Mechanical Assembly, from [25]

Using the pyramidal Berkovitch indentation tip, the reduced Modulus takes into account the elastic deformation of both the composite and the Berkovitch tip and is calculated using [26]:

$$E_r = \frac{1-v^2}{E} + \frac{1-v_i^2}{E_i},$$ (2)

where E_r is the reduced Young's Modulus and E and E_i are the Young's Modulus for the sample and indenter tip while v and v_i are the Poisson's Ratio and Poisson's Ratio of the sample and indenter tip, respectively. Further derivation to account for the geometry of the Berkovitch tip and the dynamic viscoelastic properties of polymers lead to:

$$E_c = E' + iE'',$$ (3)

where E_c is the complex modulus, E' is the storage modulus, E" is the loss modulus, and i is $\sqrt{-1}$.

To calculate hardness, the following equation is used:

$$H = \frac{P_{max}}{A(h_c)},$$

(4)

where H is the hardness, P_{max} is the maximum load, A is the contact area, and h_c is the contact depth. Figure 23 [26] shows a typical plot of load vs. indenter displacement where loading increases to the maximum load, P_{max}, and plastic deformation is shown as the curve unloads and is shown by the permanent displacement, h. Elastic recovery is shown as the difference between h and h_{max}. Four samples at a time were loaded into the stage and tested this way using the same parameters as in previous the studies of epoxy composites by Maxson [27] and Moberg [28] and outlined below (Table 2).
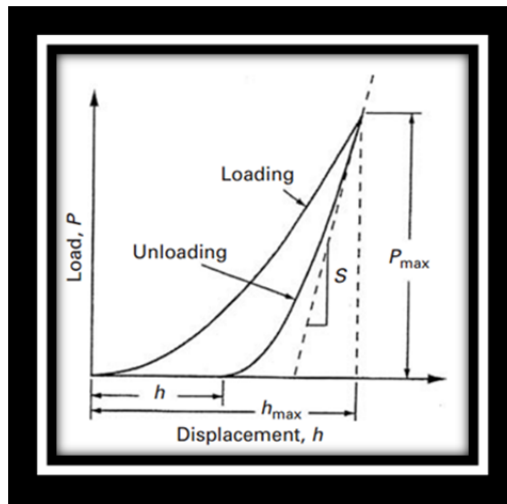

Figure 23.   Load/Unload vs. Indenter Displacement, from [26]

Table 2.   Nanoindenter Parameters

Mode	XP-Basic Modulus/Hardness at Depth
% Unload in Stiffness	50.000
Poisson's Ratio	4.0
Allowable Drift Rate	0.05 nm/s
Depth Limit	2000 nm
Peak Hold Time	10.000 s
% to Unload	90.000
Strain Rate	0.08 / s
Indents	20 point Array with 50 micron separation

D. FAILURE INDUCTION – ULTRASONIC LIQUID PROCESSOR

The Sonomechanics 1200W Ultrasonic Liquid Processor was used to induce failure in the spherical nickel nanoparticles (Figure 24). This ultrasonic transducer converts electrical energy from the integrated generator into mechanical energy in the form of ultrasonic vibrations. These vibrations are then amplified to an intensity which forms bubbles of up to 100 microns, then sent into the liquid directly from a high-gain acoustic horn, where one end of the horn is in contact with the low amplitude transducer and the other end of the horn is immersed in the liquid.

Figure 24. Sonomechanics Ultrasonic Liquid Processor

This particular machine uses a half wave barbell horn that increases the power density and can almost double the radiating area through its upper and lower output surfaces rather than a single surface from conventional converging acoustic horns (Figure 25) [29]. The failures induced in the samples result from the shear forces from the micro-jets caused by the "violent and asymmetrically imploding bubbles" emanating from the ultrasonic cavitation caused by the barbell horn into the fluid [29]. The rapid (less than a microsecond) bursts can create heat as high as 5500°C [30] and require the constant pumping of ice water into the system.
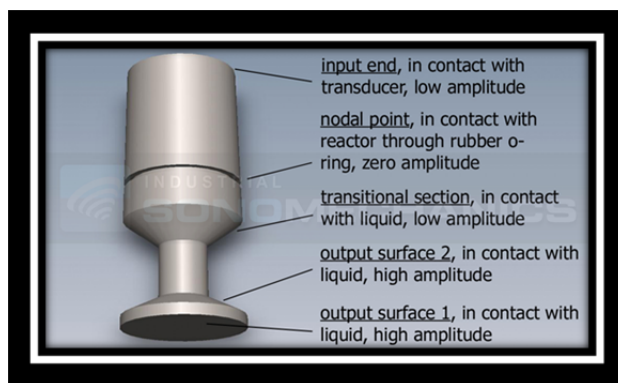
Figure 25.   Half Wave Barbell Horn, from [29]

To mitigate sample loss from evaporation due to the high heat generation and spillover from the cavitation, 370 mg of nanopowder was placed into a 20 mL vial then filled with ethanol and capped. This vial was then placed in an ice water bath set into the Ultrasonic Liquid Processor. The processor setting of 100% amplitude and 270 Watts resulted in a frequency of 19499 Hz. After one hour, the vial was emptied into an evaporation dish, set into the drying oven at 40°C, and allowed to dry, before preparing for characterization in the SEM, TEM, and XRD (Figure 26).
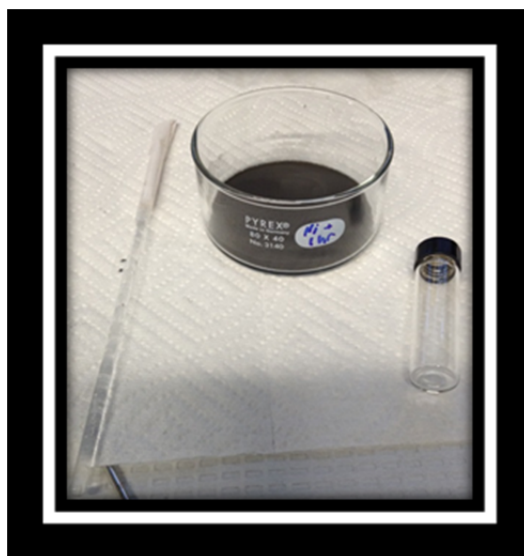
Figure 26.   Nickel Sample Post Test

III. RESULTS AND DISCUSSION

The results of the preparation and characterization (described in the previous chapter) of the samples have been organized as reiterated in Figure 27. Thus, this chapter begins with the presentation and discussion of the observations, data, calculations, and measurements generated, for: A) Nickel sample separation by particulate size; B) Generation of the nickel epoxy composites and determination of their mechanical properties; C) Failure analysis of the individual nickel nanoparticles, and; D) Use of microwave plasma methods to generate spherical nickel nanoparticles.
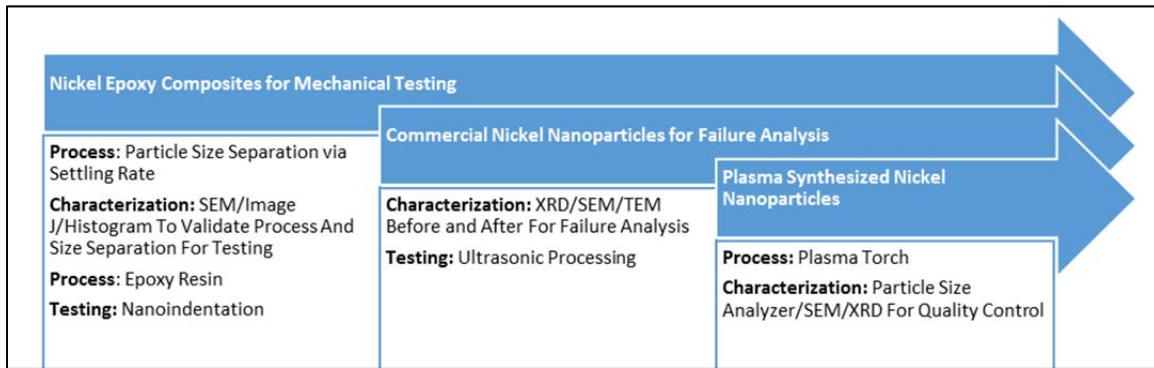

Figure 27.   Thesis results organization

A.   NICKEL EPOXY COMPOSITES

Characterization of the commercial nickel nanopowder, then particle size separation by means of settling rate technique, began prior to the inclusion into the epoxy matrix. The results of the first two separation runs showed impractically low yields for the first two samples with the majority of the nickel nanopowder in the third through fifth samples. There were enough samples from the first two runs however, to analyze in the XRD and SEM.

The XRD results revealed a pure nickel product (Figure 28) while SEM characterization clearly showed the spherical nature of the majority of nanoparticles in the commercial sample (Figures 29 and 30). These are considered positive results as the shape can be reproducible in the microwave plasma torch, however, size distribution

measurements through the ImageJ software, showed minimal differences between the first two samples, between the third and fourth samples, and an accumulation of every size and shape in the fifth sample of this first run.
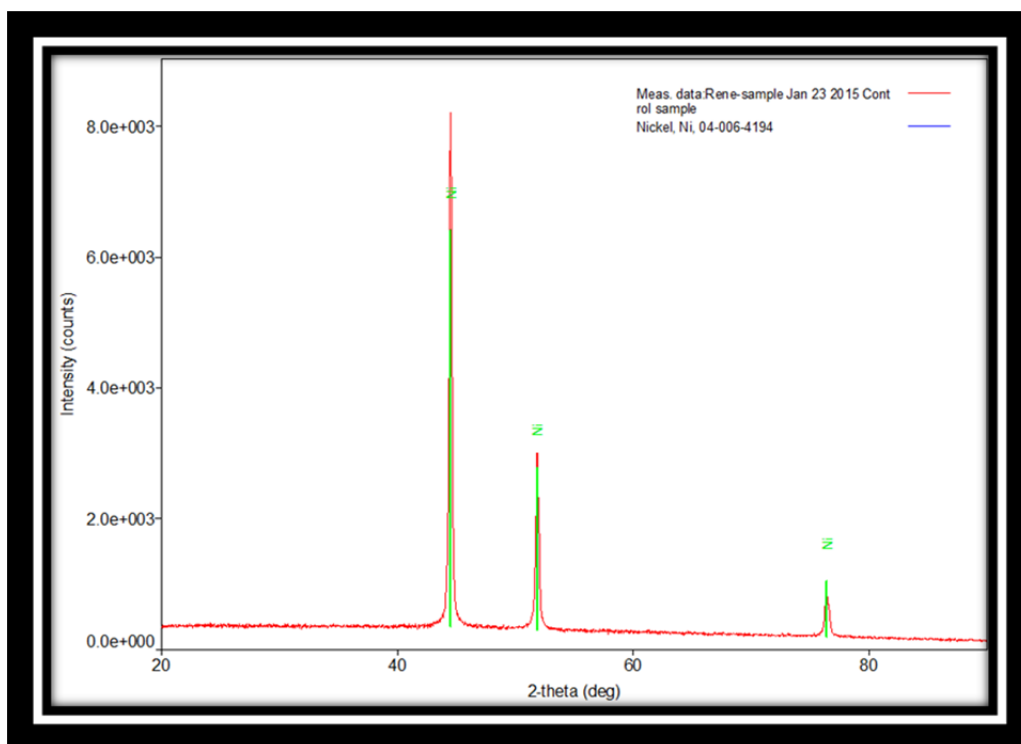

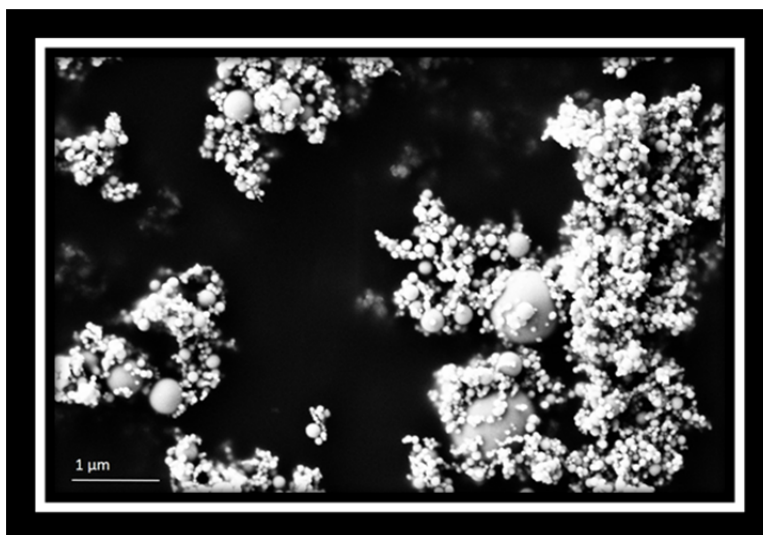Figure 28.   Diffraction Plot of Commercial Nickel Control

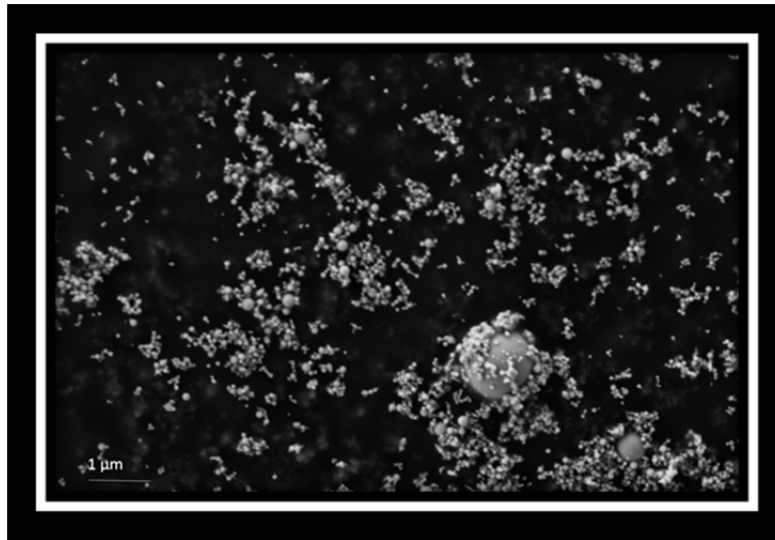Figure 29.   SEM Image of First Sample of Nickel Nanoparticles

30

Figure 30.   SEM Image of Fifth Sample of Nickel Nanoparticles

Once the timing of the runs was calibrated, the final run was completed and the samples were characterized in the SEM. These SEM images were then analyzed with ImageJ, JMP, and MS Excel, and the final size distributions were assessed (Figures 31 and 32). Results obtained by the JMP commercial software calculates the quartiles, median, and mean average values for each of the samples as well as the standard deviation.

Figure 31.   Particle Size Distribution Statistics Using JMP

31
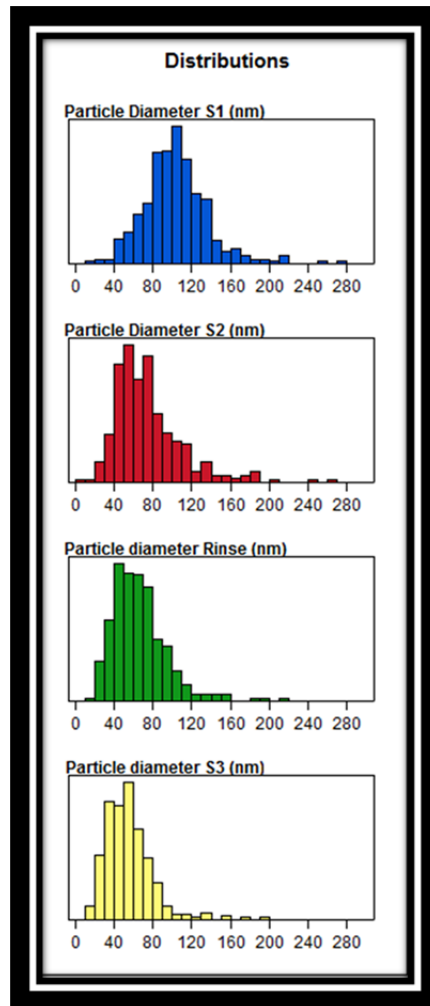
Figure 32.   JMP Size Distribution Histogram of Settling Rate Particle Separation

The four separate size distributions that resulted from this final run validate the use of settling rate for particle separation as each distribution separated distinctly. Figure 33 shows a graph relating the elapsed time in seconds to the mean particle size distribution found from the JMP histograms. Yields were as noted in Table 1. Due to the low yields for the smallest particles, the yields from the rinse sample and Sample 3 were mixed together to make an adequate layer for composite testing in the nanoindenter.

Figure 33.　Particle Size Separation by Settling Rate

Following XRD verification—to determine the purity of the nickel sample— and particle size separation, the nickel nanopowder was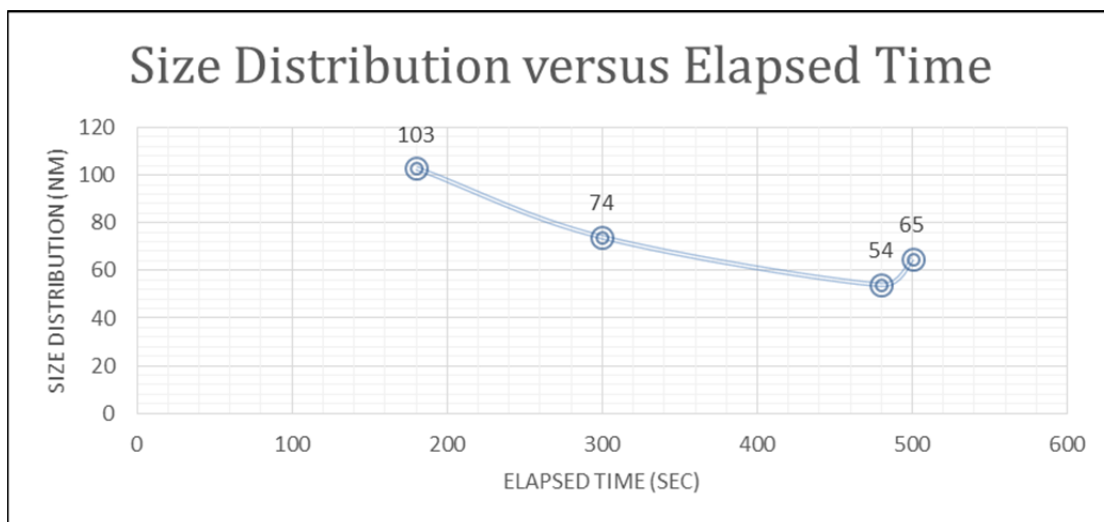 mixed with the epoxy matrix to produce the nickel epoxy composite pucks. The addition of nanoparticles to a polymer to form a particle-reinforced composite has been of particular interest over the past 20 years. Composed of the epoxy matrix to distribute the load to a single reinforcement phase consisting of only 1% of nickel nanoparticles, nanoindentation is the proper test to characterize the nickel/epoxy interface considering one goal of this thesis is to correlate the different particle sizes with rigidity and hardness.

Each of the pucks were subjected to 20 load/unload curves for a larger sample size and the general results from the nanoindenter show very low standard deviations in Young's Modulus (Elastic Modulus) and Hardness. Results show a straight Hall-Petch type relationship in the hardness and Young's modulus values; as the particle size diminishes, those values increase. For example, the Young's Modulus changes from 3.6 GPa in the bare epoxy, up to 3.74 and 3.85 GPa on nanoparticles with a median particle size of 102 and 68 nm, respectively. Each of the nanoparticle composites show moduli higher than the control (Figure 34) and normalization shows that these range from 1.2–6.1% higher than the control.
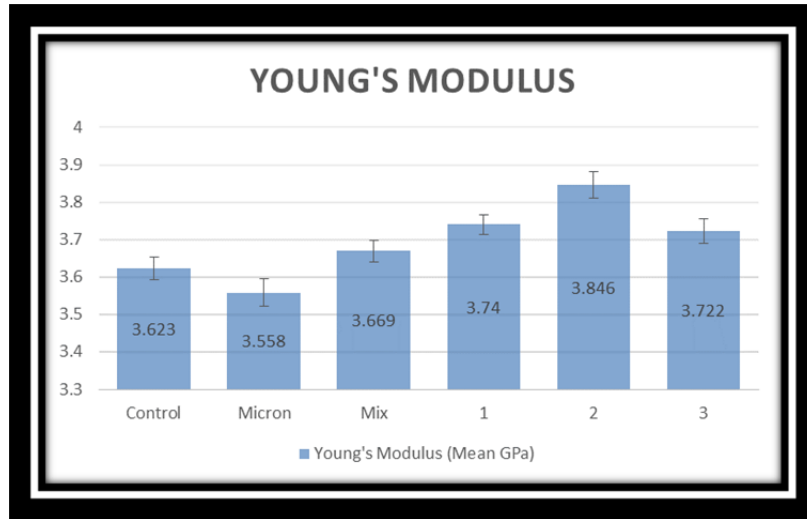
33

Figure 34.   Young's Modulus (GPa) of Composites and Standard Deviation

Meanwhile the micron-sized particles show an elastic modulus of approximately 2.8% less than the control. This is likely due to the larger interparticular spacing caused by the combination of large particle size, relatively low concentration, and sparse distribution. As per Rajagopala [18], larger particles require a higher concentration in a composite to disperse as equally as their smaller counterparts. Meanwhile, Kutvonen [19] argues that the higher surface to volume ratio of the nanoscale particles have both a higher incidence of the creation of the stronger polymer to nanoparticle connection and an increased ability to form temporary crosslinks over their micron-scale counterparts.

The hardness, or resistance of the plain epoxy puck to plastic deformation is measured at 0.193 GPa (Figure 35). For most of the samples, the trends follow that of the Young's Modulus results in the Figure above. For Sample 2, however, the hardness results show a hardness of 5.7% less than the control. Repeated nanoindentation in different areas of the composite pucks reveal similar results.
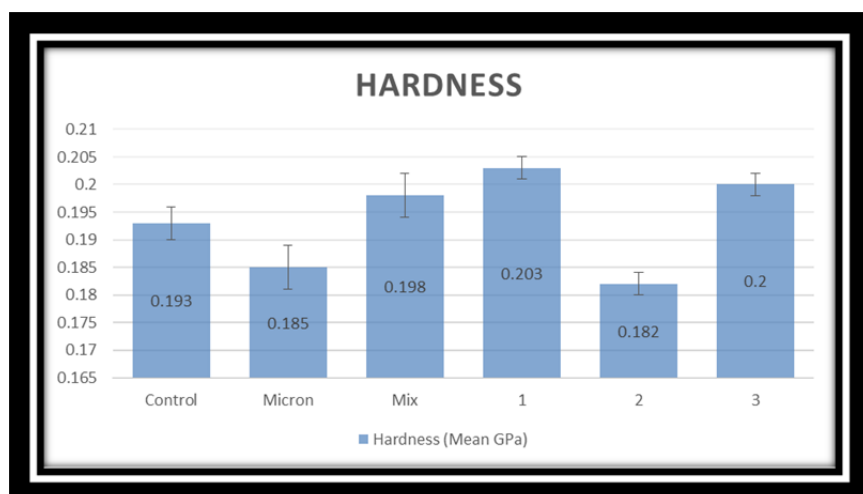
Figure 35.　Hardness of Composites (GPa) and Standard Deviation

Kutvonen et al. [19], may shed some light on the fact that Sample 2 resulted in a lesser hardness than that of the control. This smaller range of plastic deformation, coupled with a larger elastic range from the Young's Modulus graph is certainly aberrant. However, with the possibility of uneven dispersal during processing, the inclusion of the spherical nanoparticles into the polymer strands to create the strong polymer to nanoparticle connection would not occur in the areas of agglomeration. Indeed, the weak nanoparticle to nanoparticle connections would predominate in the agglomerates and actually weaken the composite. The possibility exists that the nanoindenter pressed onto a layer of agglomerates which exhibited a more rigid nature as they were supported by the polymer matrix; however, once indented, the short range to plastic deformation was inevitable.

B.　FAILURE ANALYSIS OF INDIVIDUAL NANOPARTICLES

Failure analysis of the commercial nickel nanopowder began with characterization of the nanopowder using the XRD, SEM, and TEM. The results of the XRD were shown in the previous section (Figure 28). Meanwhile SEM images revealed mostly spherical, aggregated particles with a bi-modal distribution (Figure 36). TEM images (Figures 37 and 38) and analysis (Figure 39) show spherical, defect-free nanoparticles with no signs of oxidation, and correlate with the XRD and SEM results. The bi-modal distribution revealed using the SEM is verified, while submicron and

100+ nm particles are shown, Figure 37 shows the capability to view sub-10 nm particles, their individual crystals, and grains, at high magnifications.
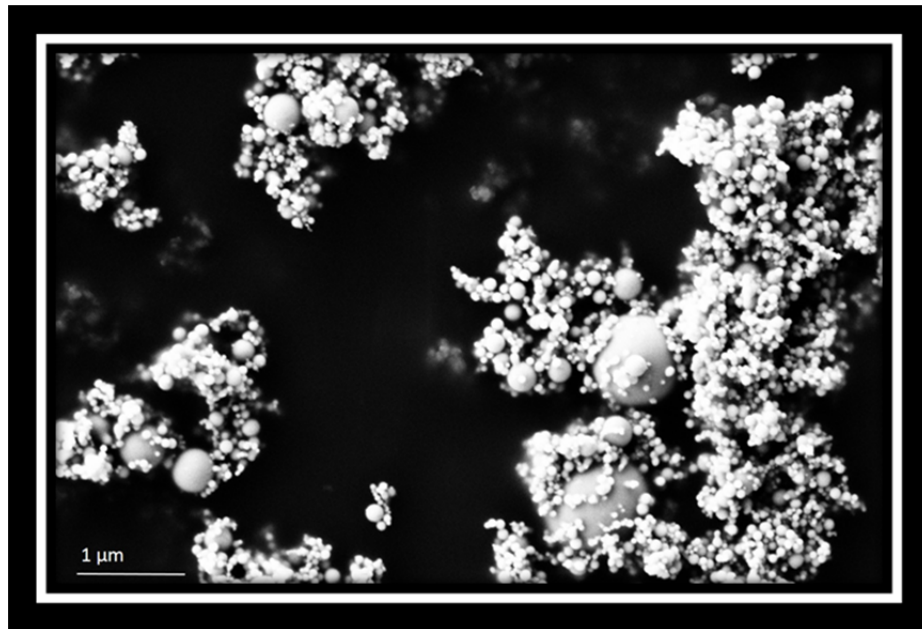

Figure 36.   SEM Image of Nickel Control Sample prior to Ultrasonic Processing
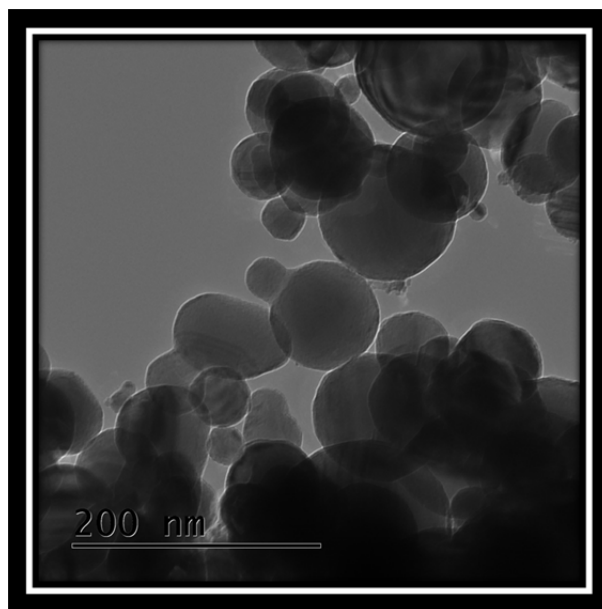

Figure 37.   TEM Image of Nickel Control
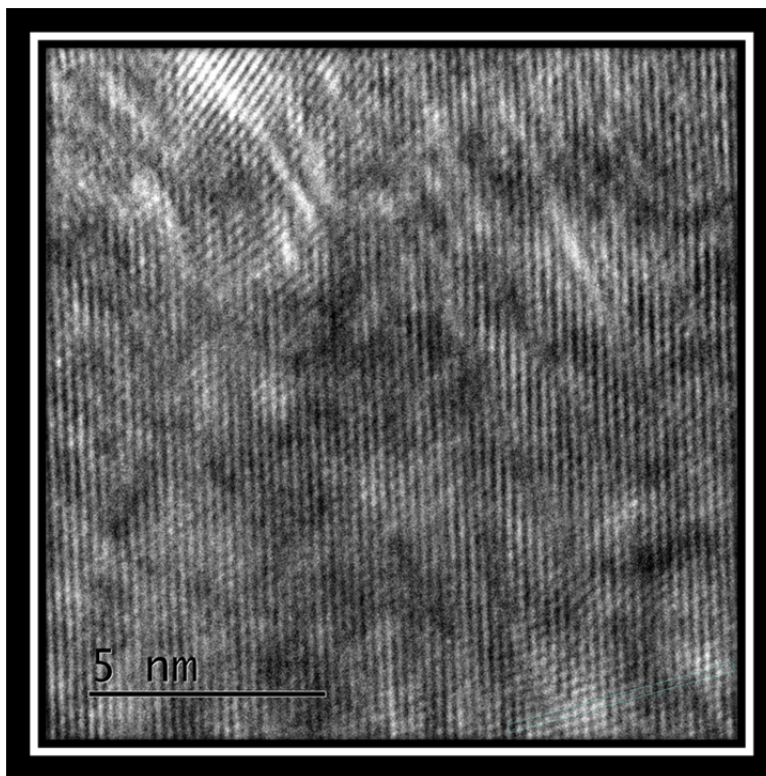
Figure 38.   Sub-10nm Nickel Particles in Control Sample

At this level of magnification, the individual crystals of the control sample can be seen as individual dots aligned in grains. The nickel lattice spacing measured with the XRD was verified using a histogram profile program (Figure 39) within the TEM image acquisition software (Digimicrograph). The peaks and valleys in the image correspond to the individual atomic columns and space between them, respectively. The 2.04 nanometers measured with the TEM measures 10 crystals and their spacing. Dividing by 10 to get the average spacing, a close match to the XRD measurement of 0.2034 nanometers for {111} spacing in pure Ni and a perfect match to the PDF Card standard is revealed.

Figure 39. TEM-measured Crystal Lattice Spacing in Nickel Control Sample

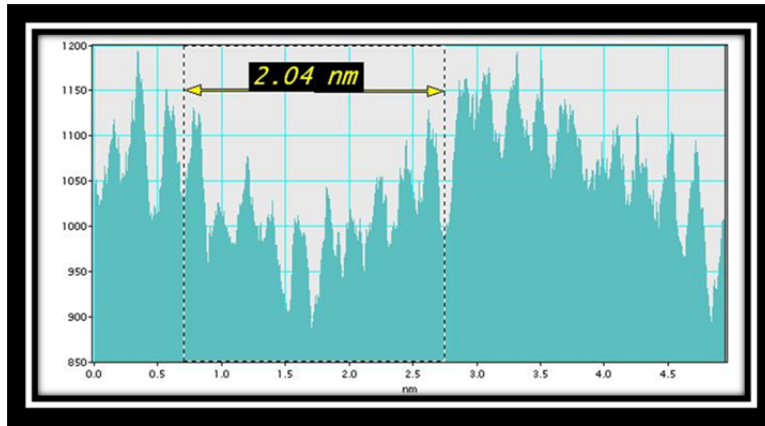Post-ultrasonic testing revealed sintering of the smallest particles and seemingly intact larger spheres. Particles sinter in the presence of heat and the surface diffusion process brings the smaller particles together. This happens in particular to nanoparticles due to the larger ratio of surface area to mass. The relatively larger surface area will absorb more energy from the system and as a mode to dissipate this energy; the smallest particles will sinter together at since their melting points are lower than their larger counterparts.

As the following figures show, the majority of whole, unoxidized, nanospheres in Figure 36 have agglomerated into what looks like a cliff wall in Figure 40. This figure also shows necking to spheres of different diameters; however the largest spheres appear unscathed and able to shed the energy from the ultrasonic processor. Meanwhile, Figure 41 shows a STEM image of what appears to be an oxide coating that surrounds the nickel nanoparticles and could be a result from the immersion in the ethanol medium and energy incurred from the ultrasonic vibrations.
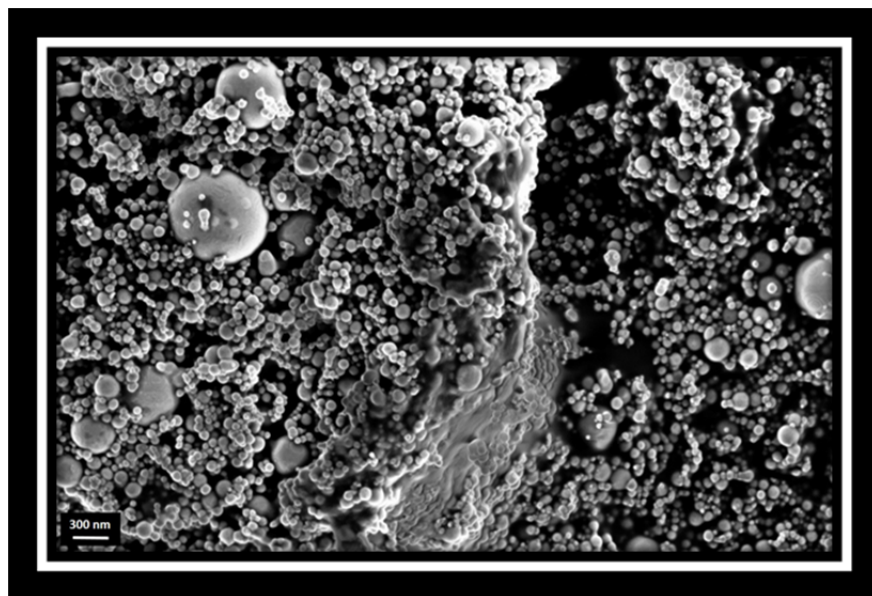
Figure 40.   SEM Image of Nickel Nanoparticles after One Hour Ultrasonic Treatment
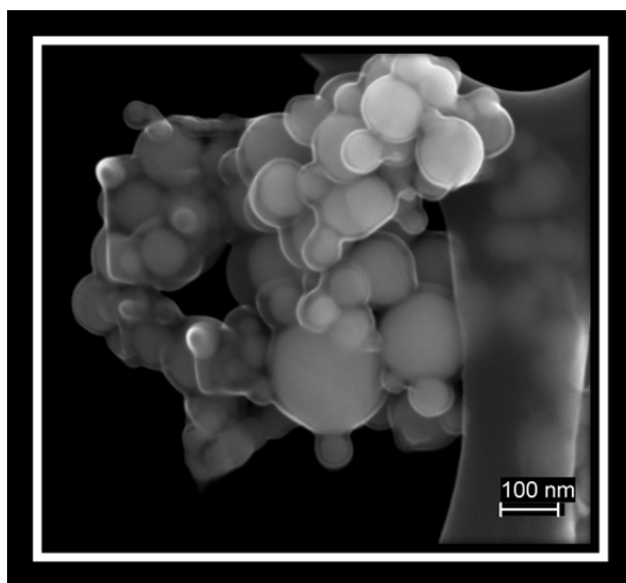
Figure 41.   STEM Image of One Hour Ultrasonically Treated Nickel

TEM images of the one hour ultrasonically-treated nickel revealed crystal twinning unseen in the control sample (Figures 42–44). According to Meyers and Chawla [26], the twinning planes occur from the atomic displacement due to the plastic deformation (Figure 45) [21]. The presence of twinning itself is indicative of applied stress and strain rates higher than if only slips were found and certainly verify the high

energies (4320 kJ) associated with the ultrasonic treatment. Greer [16] and Meyers and Chawla [26] agree that twinning can contribute to desirable properties such as increased strength and ductility. These properties result from the work-hardening that results from the segmentation of the larger planes. Once segmented, these smaller planes pin the movement of dislocations and prevent the occurrence of slips in planes perpendicular to the twin boundaries.
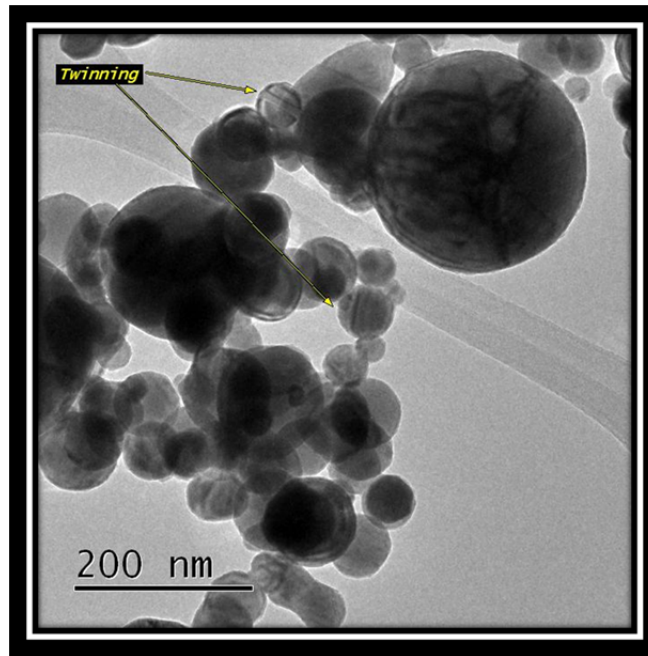
Figure 42.   Twinning of the One Hour, Ultrasonically Treated, Nickel Nanoparticles
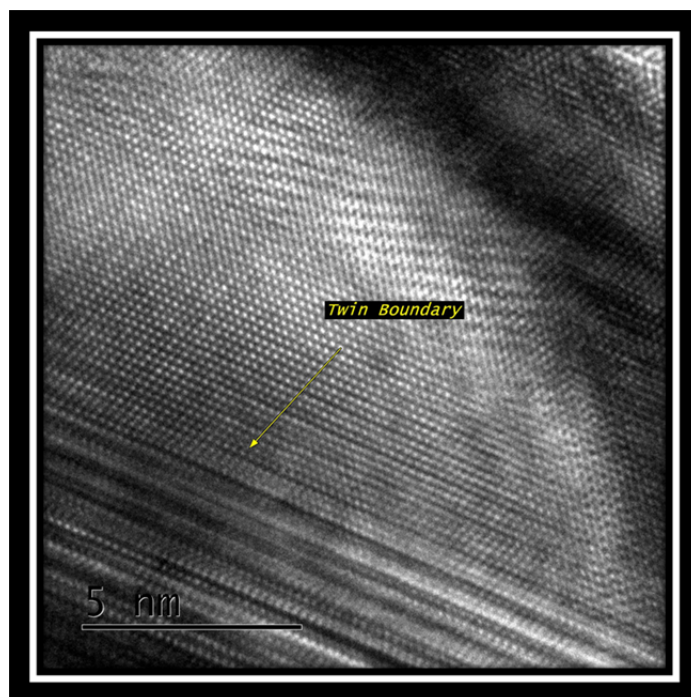
Figure 43.   Twin Boundary within One Hour, Ultrasonically Treated Nanoparticle
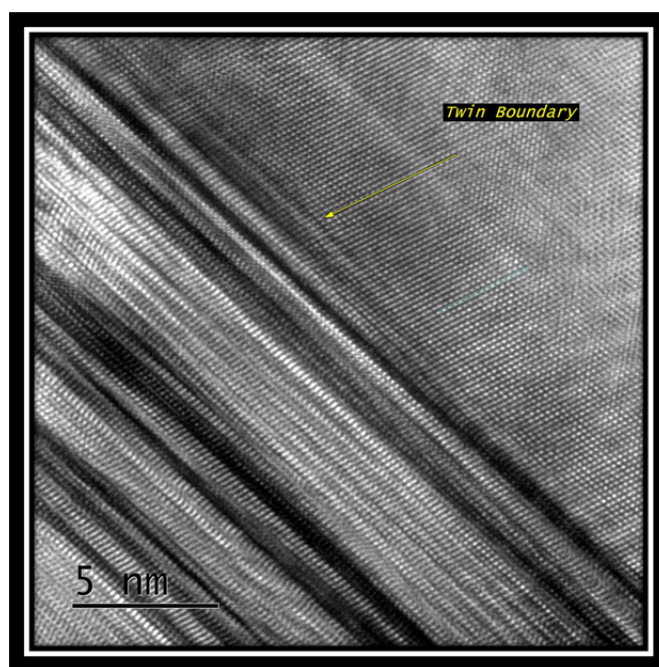
Figure 44.   Twin Boundary in Separate Nanoparticle
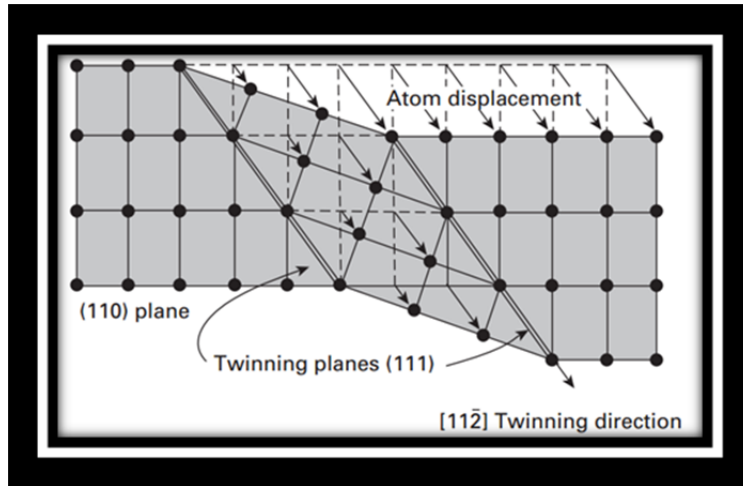
Figure 45.   Schematic of Twinning in FCC Metals, from [21]

XRD results of the ultrasonically tested samples show the presence of NiO peaks indicating the oxidation of the 30 minute sample (Figure 46); however, the XRD results for the one hour sample lacks the presence of oxidation (Figure 47) and is questionable. Immersed in an oxygen-containing ethanol medium and showing signs of sintering from the high amounts of energy, it is unlikely that the one hour sample escaped oxidation. Further investigation using the TEM showed definitive proof of oxidation for the one hour ultrasonically treated sample by closer imaging of the layer seen in the STEM image (Figure 41).
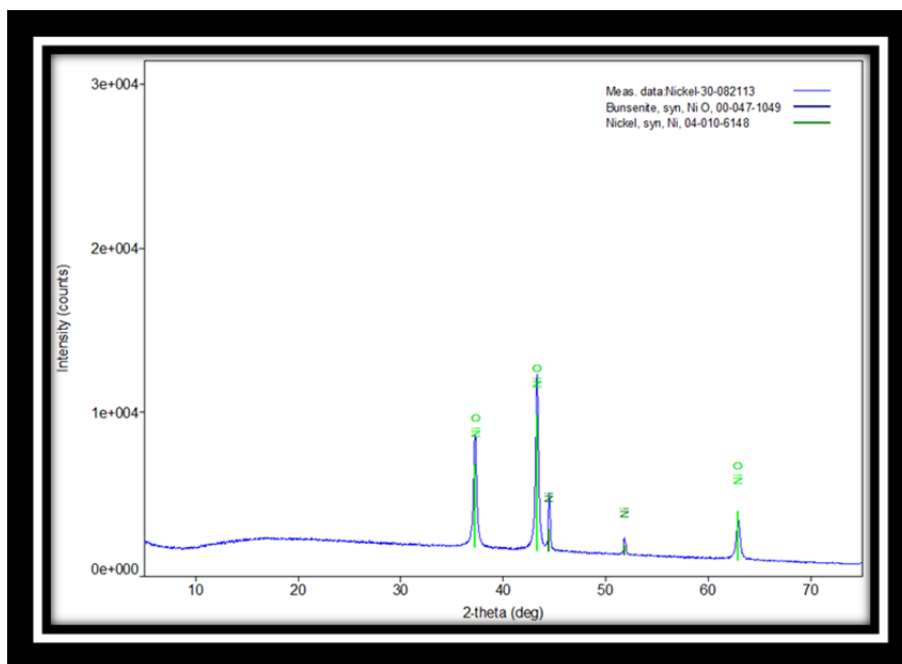
Figure 46.   Diffraction Plot of 30 Minute Ultrasonic Treated Nickel
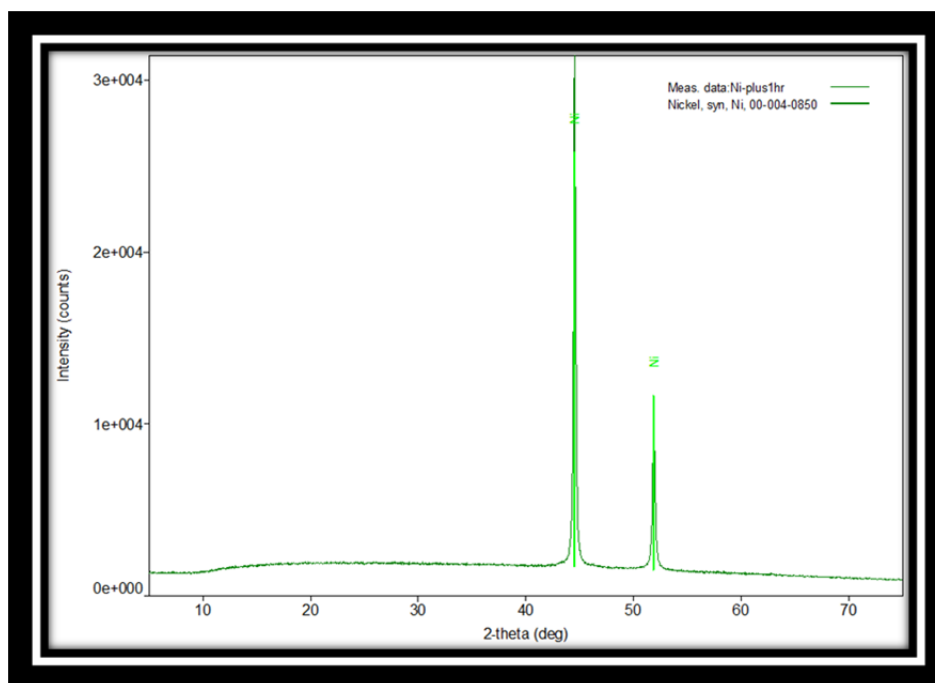
Figure 47.   Diffraction Plot of One Hour Ultrasonic Treated Nickel

The determination of the oxidation required the measurement of the crystal lattice spacing of the coating seen in Figure 48 and the comparison to the PDF Card standard in Table 3. The 2.6 nm TEM measurement of 10 crystals and their spacing matches the PDF Card standard for NiO with a single crystal spacing of 0.26 nm (Figure 49). The nickel crystal lattice spacing for the nickel nanoparticle was also measured and a three-thousandths of a nanometer deviation from the 0.204 nm standard was found (Figure 50).
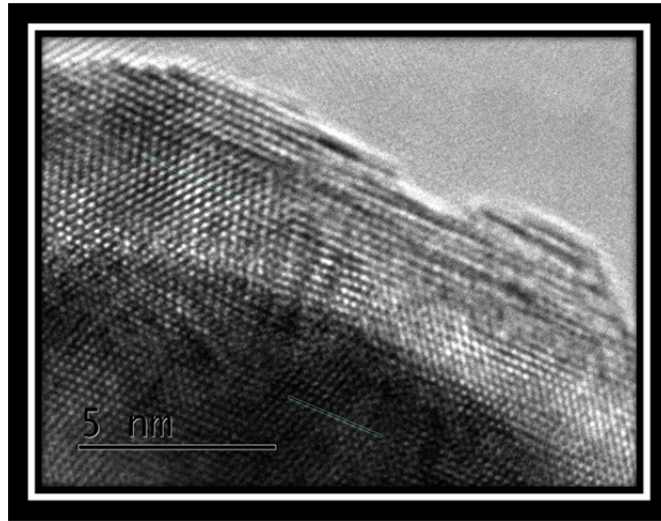
Figure 48.   Oxide Layer Surrounding Nickel Nanoparticle
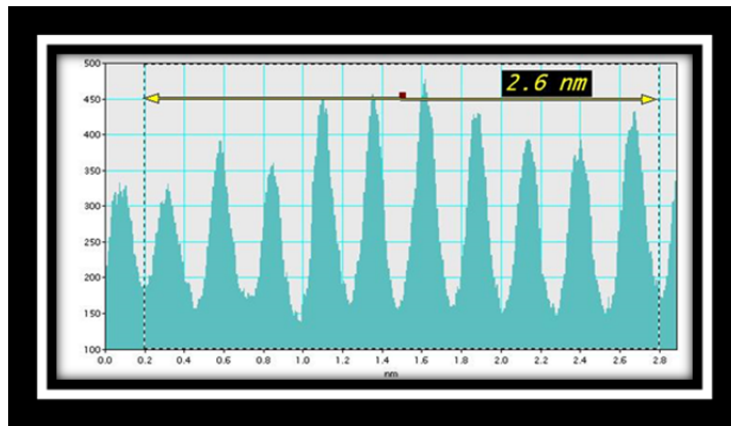
Figure 49.   Crystal Lattice Spacing of Coating over Nickel Nanoparticle
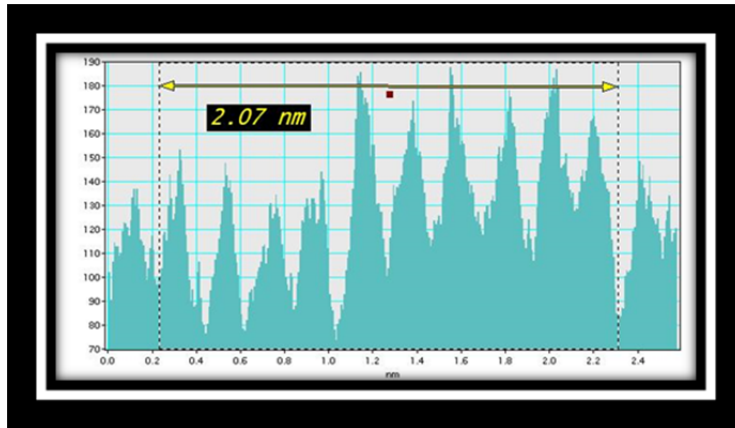
Figure 50.   Crystal Lattice Spacing of Nickel Nanoparticle under Oxide Coating

Aside from twinning and agglomerations from the smallest and most susceptible particles; fractures, dislocations, delaminations, microcracks, and other evidence of deformation were not found. The lack of these deformations may be the result of the fortuitous formation of the 2–3 nanometer thick oxide coating during ultrasonic treatment. If this oxide coating forms quickly, the protection of the smallest particles from melting and agglomerations is possible. The use of a high temperature resistant particle would also allow for the protection of the smallest particles.

The protection afforded by this oxide coating from internal and external stresses can be likened to the mechanics of biocomposites posed by Gao et al. [31], where this coating acts as a "soft wrap" to protect the nanoparticle. It protects by transferring external tensile loads on the individual particle to internal shear loads shared by the matrix and other individual particles to avoid overloads (Figure 51) [31]. Although focused on biocomposites, and specifically mineral platelets in a protein matrix (the soft wrap), Gao [31] proposes that with: 1) an optimum aspect ratio of the platelets/reinforcing particle; and 2) the right thickness and volume fraction of the protein matrix; flaws in any nanocomposite can become inconsequential. From the TEM images (Figure 52 and 53), twinning most likely occurred prior to or during the formation and expansion of the coating and as shown; the termination points for the twinning planes are at the inside of this coating. This is indicative of the strength of this oxide layer to pin

further movement of the twins, prevent further deformations and subsequent failure to the nanoparticle, and render the twinning flaws possibly inconsequential.
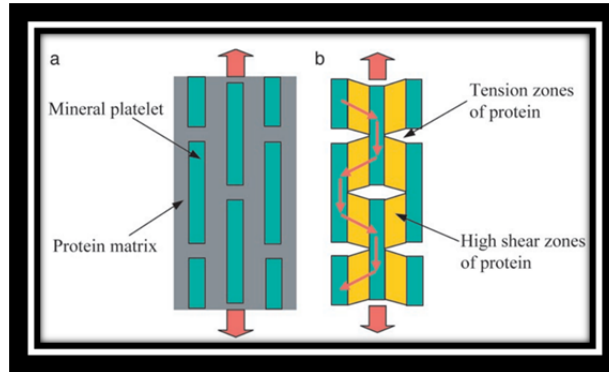
Figure 51.   Tensile Load to Shear Load Transfer in Biocomposites, from [31]
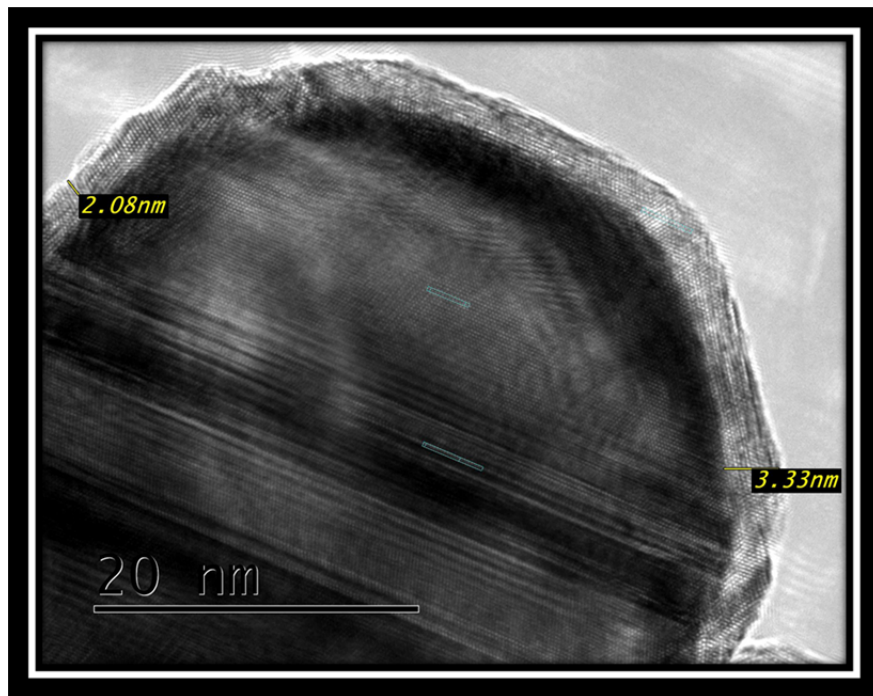
Figure 52.   Oxide Layer Thickness
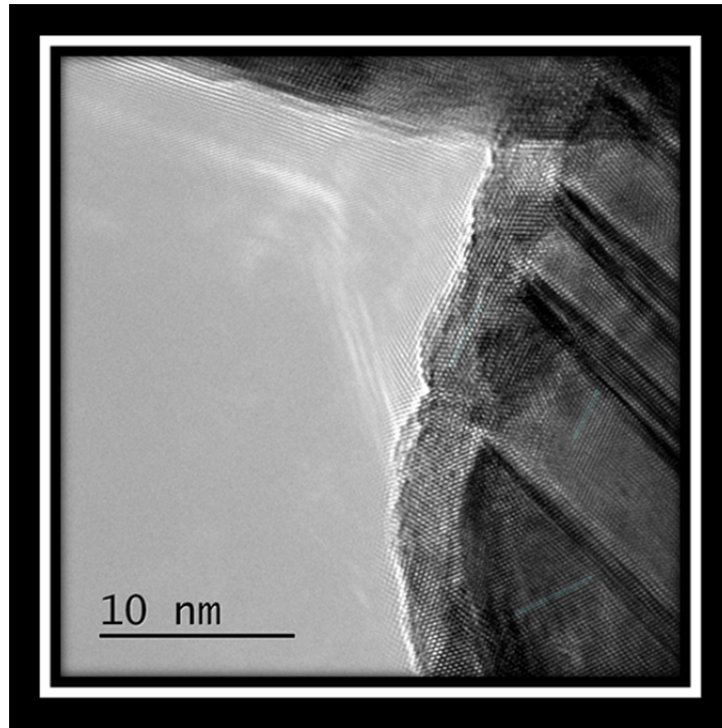
Figure 53.   Twinning Planes and Termination at the Oxide Layer

As a method for a more in-depth analysis, the crystal lattice spacing of the (111) planes of nickel were compared between each sample, the commercial control, and the PDF card standard of 0.204 nm, to determine any significant changes to the crystal lattice spacing. As a graphic example of the comparison between the samples and their corresponding planes, Figure 54 shows a section of the diffraction patterns for each of the samples. The nickel (111) planes in this figure correspond to the peaks between the 44- and 45-degree marks; as shown, each sample has a characteristic scattering intensity (height) and width.
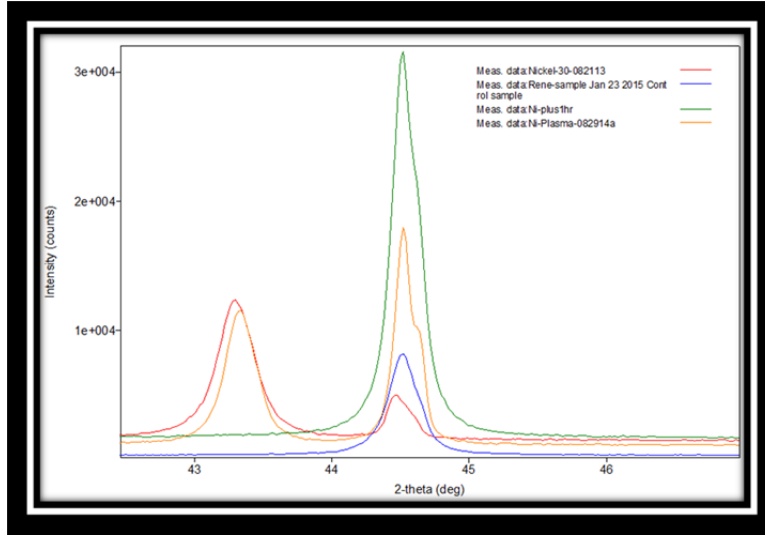
Figure 54.   XRD Ni (111) Peak Comparison

Determination of the lattice spacing begins with the equation:

$$d^2{}_{hkl} = \frac{a^2}{h^2 + k^2 + l^2},$$

(5)

where h, k, and l are the coordinate positions of the atoms in a unit cell, a is the lattice parameter, and d is the crystal lattice spacing. In this study, the focus is on the h=1, k=1, and l=1 coordinates that describe the plane (111). Substitution, rearrangement, and simplification of this equation yields the following equation for the crystal lattice spacing between the (111) planes in a FCC unit cell (d_{111}):

$$d_{111} = \frac{a}{\sqrt{3}},$$

(6)

The lattice parameters for each sample were gathered from diffraction, then refined using the Crystal Lattice Parameter refinement page on the Rigaku PDXL program. These refined parameters were then divided by $\sqrt{3}$ and tabulated in Table 3. Correlations can be seen between the plasma synthesized samples and the ultrasonically treated samples. Each of the plasma samples showed crystal lattice spacings infinitesimally smaller than that of the nickel control whereas the ultrasonically treated samples showed crystal lattice spacings minutely larger than the control. These values

48

were verified using the TEM and changes in phase were not found to correlate with lattice spacing.

Table 3.   Crystal Lattice Spacing of Ni and NiO (111) Planes

Sample	Crystal Lattice Spacing (in nm)
Plasma #082814	0.20338
Plasma #101714	0.20338
Commercial Control	0.20340
Ultrasonically Treated (1 Hour)	0.20341
Ultrasonically Treated (30 Min)	0.20361
PDF Card Standard for Nickel	0.204
PDF Card Standard for Nickel Oxide	0.26

If the oxide coated nickel nanospheres in this study are likened to composites then parallels can be formed with this study, that of Gao et al. [31], and the study of Cook et al. [32]. Cook et al. [32] find that uncoated, polyhedral, Inorganic Fullerene-type Tungsten Disulfide nanoparticles are susceptible to fractures, agglomerations, microcracks, and delamination from shock tube and ultrasonic treatment, at the vertices (Figure 55) [33]. The formation of the oxide layer in this study appears to have limited the damage incurred to the spherical nanoparticles and could be used to protect the susceptible vertices of non-spherical particles with the mechanism posed by Gao et al. [31]. While optimal thicknesses need to be researched for the different sizes of nanoparticles, the size of the particle shown in Figure 54 would benefit from the 2–3 nm layer formed in this study. With limited studies on the modification and improvement of the mechanical properties of individual nanoparticles, further study in this track would be beneficial.
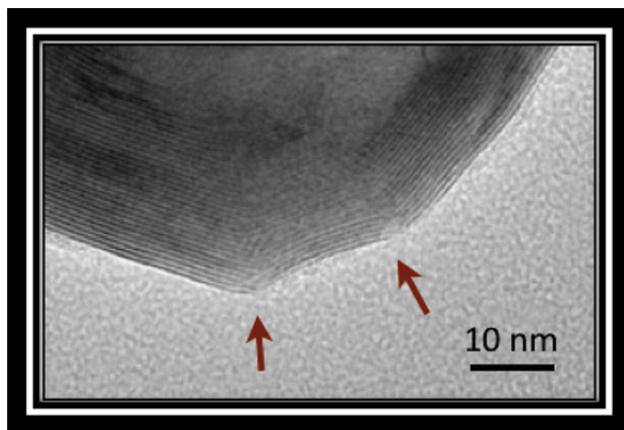
Figure 55.   Cracking at the Vertices of Polyhedral Nanoparticles, from [33]

C.   MICROWAVE PLASMA SYNTHESIS

Characterization of the plasma-produced particles was necessary to analyze the feasibility of this method in the synthesis of a more temperature resistant nanoparticle. XRD was a quick and efficient method to verify quality control procedures as the samples went from the filter directly to the XRD without having to wait the necessary desiccation time as required by the SEM. The initial plasma sample #082914 (Figure 56) showed that nickel oxide and Nickel (II) Oxide phases and are indicative of an atmospheric leak in the plasma system. This result was used to tighten quality control measures and the subsequent plasma run (sample #101714) showed success in the isolation and introduction of oxygen (Figure 57) by the use of the following techniques: the over pressurization of the system to pressures 40 torr above atmospheric pressure to prevent oxygen intrusion, the use of more stringent re-assembly methods, and the use of leak detection techniques.
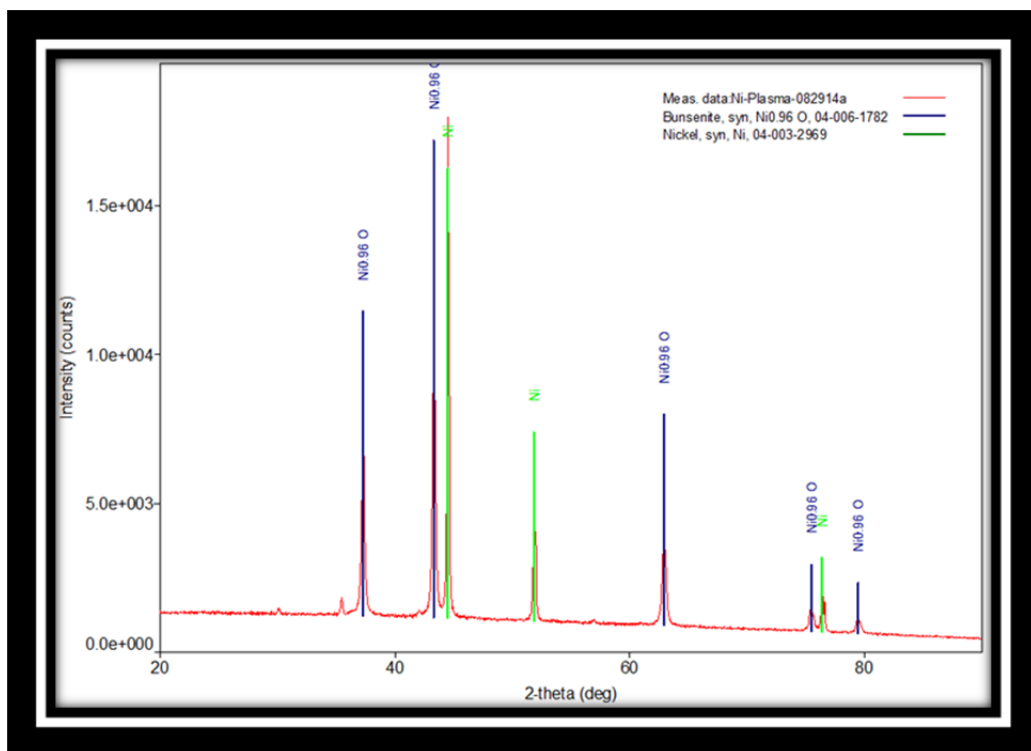
Figure 56.   Diffraction Plot of Plasma-Produced Nickel Sample #082914
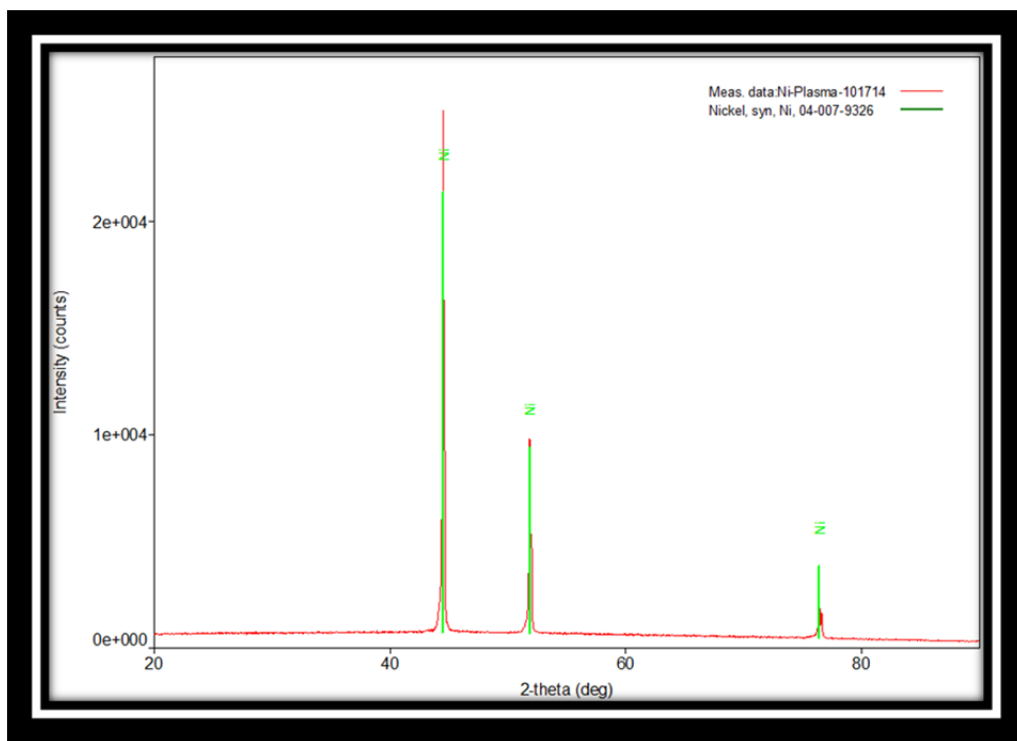
Figure 57.   Diffraction Plot of Plasma-Produced Nickel Sample #101714

The SEM was used to verify these findings and the subsequent images confirm an unoxidized spherical nickel sample in the second run (Figure 58), whereas images of the sample from the first run show cubic structures inconsistent with any samples (Figure 59). While not necessarily an indicator of oxygen, the small cubes and larger spheres represent the almost double the energy barrier required for nanoparticle cubes to grow. Aside from this aberration, crystal lattice spacings were found to be slightly smaller than that of the control and PDF standard, as noted in Table 3. Meanwhile, SEM and TEM images showed a bi-modal size distribution akin to the commercial nickel control, while TEM images showed defect-free sub-15 nanometer particles (Figures 60 and 61).
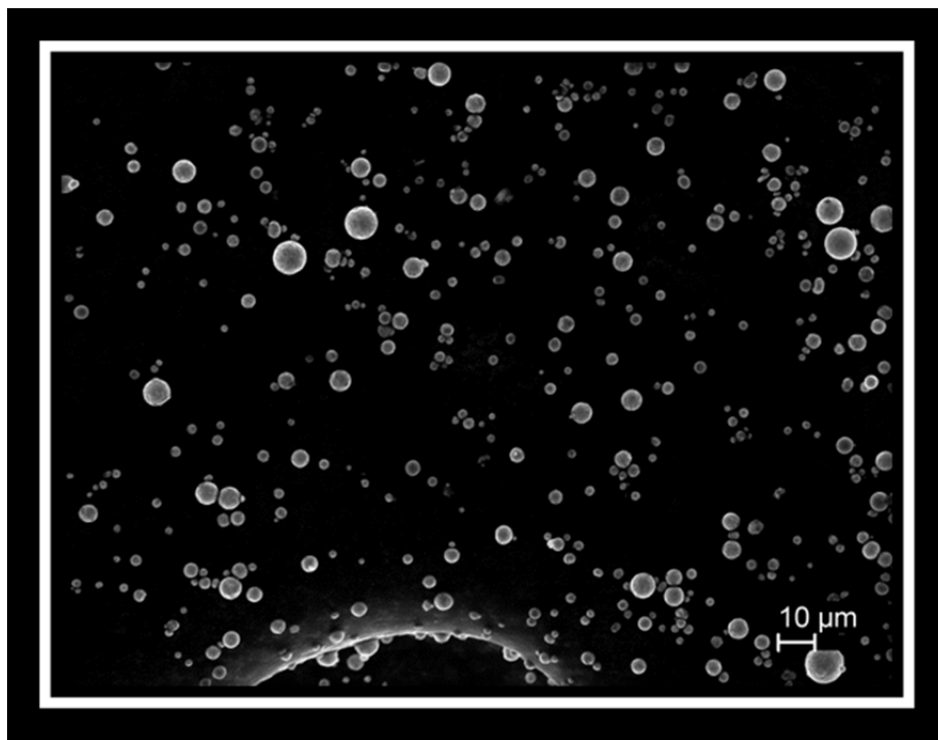
Figure 58.   Unoxidized, Micron-Sized, Spherical, Plasma-Produced, Nickel Particles
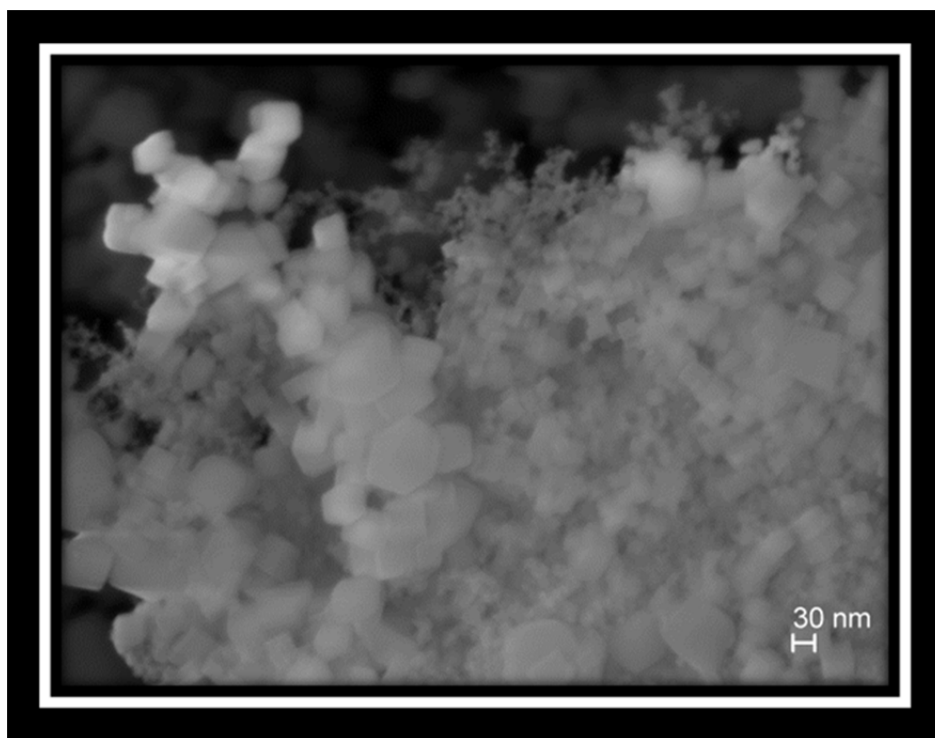
Figure 59.   Oxidized, Cubic, Plasma-Produced, Nickel Nanoparticles
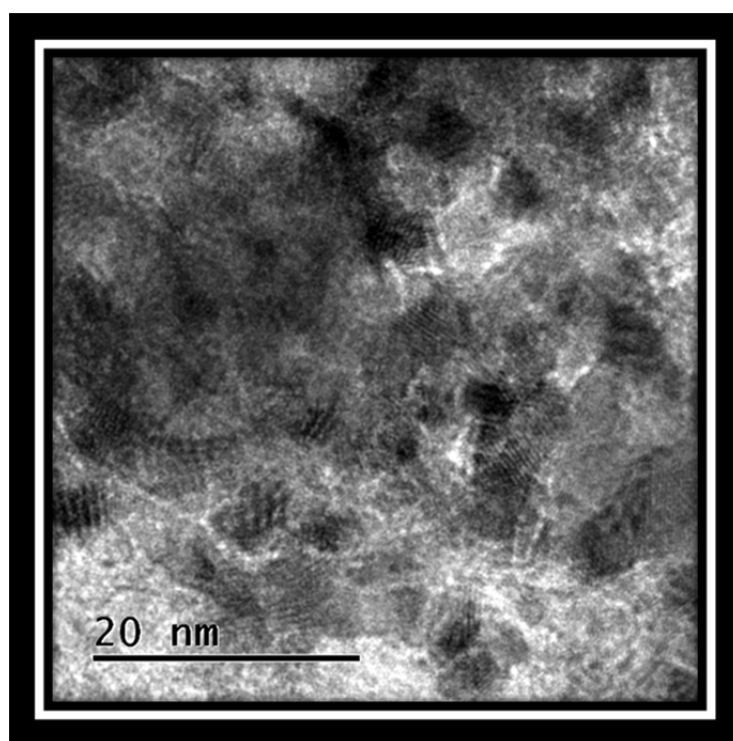
Figure 60.   Sub-20nm Plasma-Produced Nickel Particles
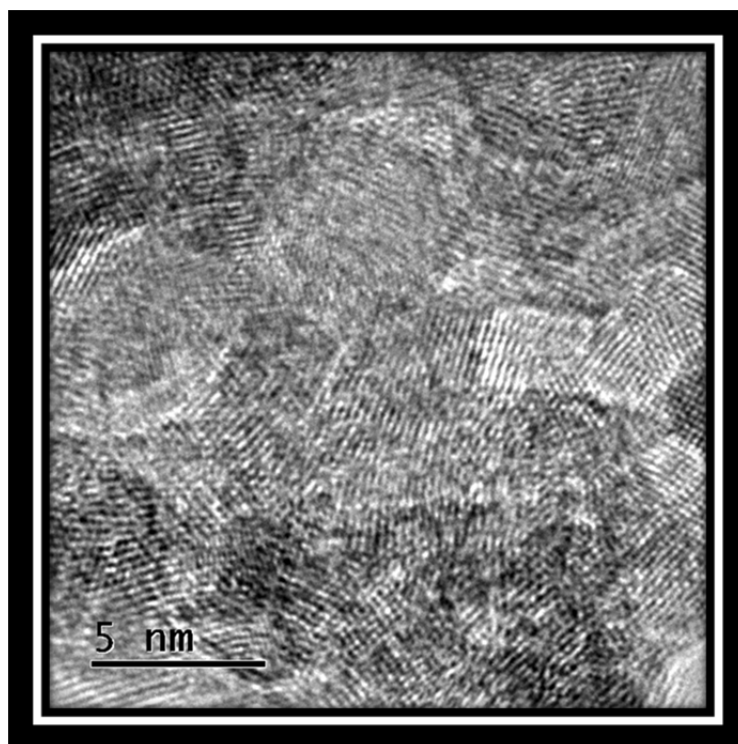
Figure 61.   Sub-10nm Plasma-Produced Nickel Particles

Particle size analysis was also conducted using the Particle Size Analyzer (PSA); a single mode size distribution of the unoxidized Plasma sample #101714 is shown in Table 4. The standard deviation was 39.6 nm with a variance of 1.571E-3 μm^2. The smallest particle size detected was 58 nm (11.11%), while the largest particle size detected was 339 nm (0.164%). The bi-modal distribution as observed through the SEM and TEM images was lost in averaging errors by the PSA. The presence of inaccuracies that accrue with PSA-specific processing and calculation lent a bias toward visual/statistical methods via SEM and TEM and image processing software such as ImageJ and JMP to achieve greater accuracy.

Table 4.   Plasma-Produced Nanoparticle Size Distribution

Average Type	Size in nanometers
Median	83.76
Mean	95.0
Mode	71.1

The production of micron- and nano-sized spherical and cubic nanoparticles by the aerosol-through-plasma microwave torch, exhibits the ability to produce various types of particles. With the need for the ability to produce nanoparticles with controllable size and morphology, and the recognized market and demand for nanotechnology, the viability of the ATP microwave torch is unrealized and not at the forefront of the leading methods and techniques [33]. Though yields and efficiency are very low, the ability to produce varied types of high-temperature and fracture resistant particles remains an interesting capability to this underutilized technique.

THIS PAGE INTENTIONALLY LEFT BLANK

IV.   CONCLUSION

Samples that contained a broad particle size distribution of spherical nickel nanoparticles were dispersed in a solvent, and separated by size according to their settling rates. The samples that resulted were dried and used as a 1% reinforcement load to an epoxy matrix to form a nanoparticle polymer composite. Composites of micron-sized nickel were also produced for comparison. The use of spherical particles helped eliminate the particle shape component in the analysis of the composite properties. The particle morphological features were analyzed using Scanning and Transmission electron microscopy and the identity of the crystalline components by X-ray diffraction.

The mechanical properties of the Ni-epoxy composites were determined by nanoindentation. Results show a straight Hall-Petch type relationship in the hardness and Young's modulus values; as the particle size diminishes, those values increase. For example, the Young's Modulus changes from 3.6 GPa in the bare epoxy, up to 3.74 and 3.85 GPa on nanoparticles with a median particle size of 102 and 68 nm, respectively. The use of micron-sized nickel particles for reinforcement of the PMC resulted in Young's Modulus values less than the bare epoxy. This behavior is attributed to the higher surface to volume ratio of the nanoscale particles that creates a larger number of bonds with the polymeric matrix than the micron-scale counterparts.

Given the large number of references in the literature, similar improvement in experimental values of hardness and Young's Modulus has been observed in other composite systems using different polymers. The merit of this section of our research was to provide experimental validation to results that previously have only been attained by modeling strategies, or those that did not distinguish between the sizes of the reinforcing particles at the nanoscale. Moreover, the ability to experimentally remove the constraint of particle shape is a major achievement since previous work by our group has proven that the edges and discontinuities on the particle surface, even at the nanoscale, act as stress concentrators.

As for the failure induced in individual nickel particulates—that is, where no composite is formed—nickel nanoparticle samples were treated as dispersions in a solvent, in an ultrasonic horn for diverse times at constant frequency and amplitude values. Postmortem analysis conducted on those samples, employed high resolution transmission electron microscopy and X-ray diffraction, and showed the effects on the particles' microstructural features and phases produced. The first observation in the treated samples was that the solvent and particles, when treated under the intense energy provided by the horn, react with each other. Indeed, a thin oxide layer (3–4 nm thick) was identified in the surface of all the particles. The peaks of NiO were also detected by XRD along the original nickel peaks. The crystal lattice features observed in the sample lead to the belief that oxidation happened in the first stages of the sample treatment; the sample size distribution seems to be the same as in the control specimen and no major agglomeration or sintering effects are seen.

Furthermore, the treated samples present an abundant number of particles in which twinning is easy to identify. The lattice distortions observed as a result of the ultrasonic treatment is arrested at the metal-oxide interface. Moreover, nanocracks, delaminations, and fractures of the particles were not observed under the conditions employed. This result is remarkable since the same treatment conditions have caused the failure of the nanostructure in other systems (ca. IF-WS$_2$, previously studied [32]).

This study provides a proof of concept on how the use of an external layer (a core-shell structure), can arrest internal defects in the samples and improve the mechanical properties of individual particulates. Molecular dynamic simulations have demonstrated that, since nanometric materials have dimensions that make impossible the use of any of the traditional strength hardening strategies and lattice defects that easily move without any mechanism to slow their motion, the mechanical properties of nanoparticles cannot be easily improved. The observations presented in this work open a path to address this particular vulnerability: the use of a shell (or maybe a vest in the case of tubular and filament nanostructures) could provide the anchor for to arrest crystal lattice discontinuities.

While deformation did occur in the form of twinning and agglomerations, further failure was stopped by the simultaneous formation of a protective nickel oxide coating. This coating pinned the ends of the twin boundaries from the inside while helping distribute loads coming from the outside. The twins themselves served to hamper the movement of dislocations perpendicular to the twin boundaries.

As an attempt to provide a way to generate highly spherical nanoparticles, with and without a shell, we employed a microwave plasma torch system. The particles generated by the system have a bimodal size distribution; with a large component below 50 nm and a second section of submicron spheres. The production yields are smaller than alternative techniques but the particles produced, as confirmed by high resolution transmission electron microscopy, are spherical and defect free. This approach is recommended to conduct future studies in this line of research.

In summary, we successfully addressed all the objectives of this thesis presented in the introductory chapter of this thesis and found a strategy to improve nanoparticle properties. These protective mechanisms could yield composite nanoparticles with novel uses; such as long-lasting dry lubricants, shock absorbing materials for personal and systems protection, or coatings for other specific needs. Synthesis of the core-shell structures appears inexpensive and, if combined with plasma synthesis procedures, could yield temperature resistant, mechanically-resilient nanoparticles, headed for ubiquitous usage.

The suggested next steps for this research are to produce diverse core-shell structures and test the properties of both the individual particulates and their epoxy composites.

THIS PAGE INTENTIONALLY LEFT BLANK

LIST OF REFERENCES

[1]   National Nanotechnology Initiative. "*Nanotechnology 101*" [Online]. Available: http://nano.gov/nanotech-101.

[2]   G. Cao, *Nanostructures and Nanomaterials*. London, UK: Imperial College Press, 2004.

[3]   R. Craig, *Mechanics of Materials*. Hoboken, NJ: Wiley, 2011.

[4]   Anonymous "United States Special Operations Command Small Business Innovation Research (SBIR)," pp. 1–10, 2013.

[5]   D. Ratner and M. Ratner, *Nanotechnology: A Gentle Introduction to the Next Big Idea*. Upper Saddle River, NJ: Prentice Hall, 2002.

[6]   M. Akbulut et al., "Forces between surfaces across nanoparticle solutions: Role of size, shape, and concentration," *Langmuir*, vol. 23, pp. 3961–3969, Mar, 2007.

[7]   R. Balaguru, and B. Jeyaprakash. (2014) "Melting points, mechanical properties of nanoparticles and Hall Petch relationship for nanostructured materials." [Online]. Available: http://nptel.ac.in/courses/115106076/Module%2010/Module%2010.pdf.

[8]   S. Kotrechko et al., "Peculiarities of plastic deformation and failure of nanoparticles of b.c.c. transition metals," *Materials Structure & Micromechanics of Fracture V*, vol. 567–568, pp. 65–68, 2008.

[9]   H. Viet et al., "Synthesis and optical properties of water soluble CdSe/CdS quantum dots for biological applications." *Advances in Natural Sci: Nanoscience and Nanotechnol.* 3, no. 025017 pp. 1–7, 2012.

[10]   U. Wiedwald and P. Ziemann, "Preparation, properties and applications of magnetic nanoparticles," *Bielstein J. Nanotech*, vol. 1, pp. 21–23, 2010.

[11]   S. Mørup et al., "Magnetic interactions between nanoparticles," *Beilstein J. Nanotechnol.,* vol. 1, pp. 182–190, 2010.

[12]   J. Lue, "Physical properties of nanomaterials," *Encyclopedia of Nanoscience and Nanotechnol.* vol. X, pp. 1–46, 2007.

[13]   Y. Ivanisenko et al., "Variation of the deformation mechanisms in a nanocrystalline Pd–10 at. % Au alloy at room and cryogenic temperatures," *Int. J. Plasticity*, vol. 60, pp. 40–57, 2014.

[14]   L. Wang et al., "In situ experimental mechanics of nanomaterials at the atomic scale," *NPG Asia Materials*, vol. 5, pp. 1–11, 2013.

[15]   R. Goldstein and N. Morozov, "Mechanics of deformation and fracture of nanomaterials and nanotechnology," *Physical Mesomechanics,* vol. 10, pp. 235–246, 2007.

[16]   J. Greer, "Nanotwinned metals: It's all about imperfections," *Nature Materials,* vol. 12, pp. 689–690, Aug. 2013.

[17]   T. Nieh, "Hall-Petch relation in nanocrystalline solids," *Scripta Metallurgica Et Materialia*, vol. 25, pp. 955–956,957,958, Apr. 1991.

[18]   R. Rajagopalan. (2015). *"Why Nanocomposites?"*[Online]. Available: http://www.ramaseshan.com/Whynanocomposite.php.

[19]   A. Kutvonen et al., "Influence of nanoparticle size, loading, and shape on the mechanical properties of polymer nanocomposites," *J. Chem. Phys*., vol. 137, pp. 214901, Dec. 2012.

[20]   D. Young, "Phase diagrams of the elements," Lawrence Livermore Laboratory, Univ. California, Livermore, 1975.

[21]   The Essential Chemical Industry. (2014). *Ethanol* [Online]. Available: http://www.essentialchemicalindustry.org/chemicals/ethanol.html.

[22]   J. Phillips et al., "Review: engineering particles using the aerosol-through-plasma method," *IEEE Trans. Plasma Sci*, vol. 37, pp. 726–739, Jun. 2009

[23]   T. Lambert et al., "Graphite oxide as a precursor for the synthesis of disordered graphenes using the aerosol-through-plasma method," *Elsevier Carbon*, vol. 48, pp. 4081–4089, 2010.

[24]   *LA-960 Laser Particle Size Analyzer How Laser Diffraction Works*, Horiba Instr. Inc., Irvine, CA, 2015. Available: http://www.horiba.com/us/en/scientific/products/particle-characterization/particle-size-analysis/details/la-960-laser-particle-size-analyzer-20235/.

[25]   *Agilent Nano Indenter G200 Data Sheet,* Agilent Technol, Santa Clara, CA, Available: http://cp.literature.agilent.com/litweb/pdf/5990–4172EN.pdf.

[26]   M. Meyers and K. Chawla, *Mechanical Behavior of Materials*. New York: Cambridge University Press, 2009.

[27]   A. Maxson, "Novel synthesis and characterization of inorganic fullerene type WS2 and graphene hybrids," M.S. Thesis, Dept. MAE, NPS, Monterey, CA, 2013.

[28]   M. Moberg, "Carbon fiber and tungsten disulfide nanoscale architectures for armor applications," M.S. Thesis, Dept. MAE, NPS, Monterey, CA, 2012.

[29]   *Barbell Horn Ultrasonic Technology*, Industrial Sonomechanics., New York, NY, Available:http://sonomechanics.com/technology/barbell_horn_ultrasonic_technology/.

[30]   K. Suslick, "The chemical effect of ultrasound," *Scientific American*, vol. February 1989, pp. 80–86, Feb. 1989.

[31]   H. Gao et al., "Materials become insensitive to flaws at nanoscale: Lessons from nature,"*PNAS,* vol. 100, pp. 5597–5600, May, 2003.

[32]   J. Cook et al., "Microstructural study of IF-WS2 failure modes," *Inorganics*, vol. 2, pp. 377–395, Jul. 2014.

[33]   Z. Libor and Q. Zhang, "The synthesis of nickel nanoparticles with controlled morphology and SiO2/Ni core-shell structures," *Materials Chem and Physics*, vol. 114, pp. 902–907, 2009.

THIS PAGE INTENTIONALLY LEFT BLANK

INITIAL DISTRIBUTION LIST

1.	Defense Technical Information Center
	Ft. Belvoir, Virginia

2.	Dudley Knox Library
	Naval Postgraduate School
	Monterey, California